

Banner appropriate to article type will appear here in typeset article

Sparse space-time resolvent analysis for statistically-stationary and time-varying flows

Barbara Lopez-Doriga¹ †, Eric Ballouz², H. Jane Bae³, and Scott T. M. Dawson¹

¹Mechanical, Materials, and Aerospace Engineering Department, Illinois Institute of Technology, Chicago, IL 60616, USA

²Mechanical and Civil Engineering, California Institute of Technology, Pasadena, CA, 91125, USA

³Graduate Aerospace Laboratory, California Institute of Technology, Pasadena, CA, 91125, USA

(Received xx; revised xx; accepted xx)

Resolvent analysis provides a framework to predict coherent spatio-temporal structures of largest linear energy amplification, through a singular value decomposition (SVD) of the resolvent operator, obtained by linearizing the Navier–Stokes equations about a known turbulent mean velocity profile. Resolvent analysis utilizes a Fourier decomposition in time, which has thus-far limited its application to statistically-stationary or time-periodic flows. This work develops a variant of resolvent analysis applicable to time-evolving flows, and proposes a variant that identifies spatio-temporally sparse structures, applicable to either stationary or time-varying mean velocity profiles. Spatio-temporal resolvent analysis is formulated through the incorporation of the temporal dimension to the numerical domain via a discrete time-differentiation operator. Sparsity (which manifests in localisation) is achieved through the addition of an l_1 -norm penalisation term to the optimisation associated with the SVD. This modified optimization problem can be formulated as a nonlinear eigenproblem, and solved via an inverse power method. We first demonstrate the implementation of the sparse analysis on statistically-stationary turbulent channel flow, and demonstrate that the sparse variant can identify aspects of the physics not directly evident from standard resolvent analysis. This is followed by applying the sparse space-time formulation on systems that are time-varying: a time-periodic turbulent Stokes boundary layer, and then a turbulent channel flow with a sudden change in pressure gradient. We present results demonstrating how the sparsity-promoting variant can either change the quantitative structure of the leading space-time modes to increase their sparsity, or identify entirely different linear amplification mechanisms compared to non-sparse resolvent analysis.

Key words:

1. Introduction

Despite the highly nonlinear nature of turbulent fluid flows, linearised analyses of the governing Navier–Stokes equations have proven to be effective at capturing several pertinent

† Email address for correspondence: blopezdorigacostales@hawk.iit.edu

Abstract must not spill onto p.2

properties of such systems. Resolvent analysis, first applied as a model for turbulent pipe flow (McKeon & Sharma 2010), has been informative in other problems that involve wall-bounded turbulence, such as the prediction of hairpin structures (Sharma & McKeon 2013), interscale interactions (McKeon 2017), spatio-temporal flow statistics (Towne *et al.* 2020), and the identification of coherent structures in turbulent jets (Lesshafft *et al.* 2019; Pickering *et al.* 2021), airfoils (Yeh & Taira 2019) supersonic boundary layers (Bae *et al.* 2020*a,b*) and turbulent rectangular duct flows (Lopez-Doriga *et al.* 2022). This framework has further been applied for the estimation of flow states (Gómez *et al.* 2016; Beneddine *et al.* 2017; Symon *et al.* 2019; Illingworth *et al.* 2018), the prediction of coherent structures (Abreu *et al.* 2020; Tissot *et al.* 2021) and statistical quantities and scalings (Hwang & Cossu 2010; Zare *et al.* 2017; Towne *et al.* 2020), designing control strategies for drag reduction (Luhar *et al.* 2014; Toedtli *et al.* 2019), and modelling the effect of complex surfaces (Luhar *et al.* 2015; Chavarin & Luhar 2019). The broad applicability of such linearised analysis relies on (and can be seen as evidence to infer) the importance of linear amplification mechanisms in the generation and evolution of empirically-observed coherent structures within turbulent flows, such as include near-wall streaks (Kline *et al.* 1967), hairpin vortices (Theodorsen 1952; Head & Bandyopadhyay 1981), superstructures (Kim & Adrian 1999), and a range of other coherent features described in Jiménez (2018).

The linearised analyses discussed thus far assume that the linear system under investigation is time-invariant, as is the case when the underlying flow is statistically stationary. The recently-developed harmonic resolvent analysis (Padovan *et al.* 2020; Padovan & Rowley 2022) enables the resolvent framework to extend to statistically time-periodic flows, enabling cross-frequency analysis capturing triadic interactions between a time-periodic base flow and fluctuations about this mean state at other frequencies. In the context of flow control over a periodically plunging cylinder, Lin *et al.* (2023) utilizes a Lyapunov—Floquet transformation to map the corresponding linear time-periodic system to a time-invariant equivalent, enabling the application of standard resolvent analysis methods.

Whether considering a statistically-stationary or a time-periodic mean state, the methods discussed thus far consider a Fourier decomposition in time. Typically, this involves identifying the forcing (input) and response (output) structures corresponding to largest energy amplification by the linearized system (represented by the resolvent operator). While this decomposition arises naturally for such methods, it can potentially obscure the intermittent nature of velocity fluctuations present in turbulent flows. Alternative linear analyses methods can be similarly restrictive, with asymptotic stability analysis also identifying eigenmodes each associated with a single (possibly complex) frequency. Conversely, transient growth analysis (Böberg & Brösa 1988; Butler & Farrell 1992; Reddy & Henningson 1993; Schmid 2007) considers the unforced response to a specific initial condition, corresponding to maximal energy growth over a specified time horizon. This again is unrealistic for systems subject to continuous perturbations (Jovanović & Bamieh 2005), though such analysis has been used in turbulent flows, such as to predict the emergence of near-wall streamwise streak (Del Alamo & Jimenez 2006) and vortices (Schoppa & Hussain 2002) in wall-bounded turbulence. To overcome these limitations, here we introduce a space-time formulation of the resolvent operator that is firstly applicable to non-statistically-stationary systems with an arbitrarily time-varying mean profile, and secondly allows for the identification of optimal input and output trajectories that can have arbitrary time dependence. This builds upon preliminary work first reported in Lopez-Doriga *et al.* (2023). While not explored here, related work also considers explicitly replacing the Fourier transform used in standard resolvent analysis with a wavelet transform (Ballouz *et al.* 2023, 2024).

This generalization of operator-based decompositions to enable non-Fourier temporal modes is somewhat analogous to efforts to similarly generalize data-driven proper orthogonal

decomposition POD methodology to identify intermittent behavior in turbulent flows, such as the conditional POD formulated in Schmidt & Schmid (2019), and time-windowed space-time POD described in Frame & Towne (2022). Note that spectral POD (Towne *et al.* 2018) has also been recently generalized for time-periodic systems using cyclostationary analysis (Heidt & Colonius 2023).

Methods to identify nonmodal linear energy amplification such as resolvent or transient growth analysis involve computing the leading singular values and vectors of an appropriately-defined linear operator. The singular value decomposition, by design, is defined as an optimisation problem that involves an l_2 -energy norm. In the context of resolvent analysis, this optimization problem relates to the energy ratio between input and output flow states, and naturally yields spatio-temporal structures that are Fourier modes in time. Here, we consider modifications to the standard optimization problem that yield alternative temporal functions, which are inclined to be localised in time. This is achieved by incorporating an l_1 norm term into the optimisation problem. The use of l_1 norms to promote localisation and/or sparsity has origins in compressive sensing (Candès & Wakin 2008)

In the context of fluid mechanics, sparsity-promoting methods have been utilised for developing reduced-complexity models across a number of contexts. These include the identification of sparse nonlinear reduced-order models (Brunton *et al.* 2016; Loiseau & Brunton 2018; Rubini *et al.* 2020), the selection of a sparse set of active dynamic modes (Jovanović *et al.* 2014), and in reconstruction of temporal spectral content from data that is under-resolved in time (Tu *et al.* 2014). Recently, sparsity promoting methods have also been incorporated in the resolvent analysis framework in Skene *et al.* (2022), where they are used to identify spatially-localized forcing modes, which can be more directly useful for actuator placement in flow control applications. In Skene *et al.* (2022), a Riemannian optimization process is used to solve an l_1 -based optimisation problem, following a similar approach used by Foures *et al.* (2013) to identify spatially-localised structures in transient growth analysis. The present work is similarly motivated, though we focus here on achieving localisation in time as well as space. We also use a different formulation of the optimisation problem, which allows for a balance between l_1 and l_2 norm contributions.

The structure of the paper is as follows. A discussion of the fundamentals of pseudospectral analysis and the wall-normal derivation of the governing equations, along with the space-time form of the resolvent operator, and a description of the algorithm that promotes sparsity on the resolvent modes are presented in §2. The main results of our investigation are discussed in §3: the sparse formulation of the standard resolvent operator is applied in the streamwise and spanwise directions of a turbulent channel flow in §3.2; and the space-time and sparse space-time formulations of the resolvent operator are applied on a turbulent channel flow in §3.3; a turbulent Stokes boundary layer in §3.4; and a channel flow with sudden lateral pressure gradient in §3.5. Finally, we discuss the main findings and future prospects of our investigation in §4.

2. Methodology

This section begins with a brief overview of the fundamentals of pseudospectral analysis of linear operators in §2.1. This is followed by a derivation of the resolvent formulation of the incompressible Navier–Stokes equations in wall-normal velocity and vorticity variables in §2.2, assuming homogeneity in both the spatial and temporal dimensions. This is followed by the development of a space-time resolvent operator where homogeneity is not assumed in the temporal dimension in §2.3, also in wall-normal velocity and vorticity variables. Following

this, §2.4 introduces a formulation of resolvent analysis that promotes sparsity on the optimal resolvent modes.

2.1. Pseudospectral analysis of linear operators

Let us consider a dynamical system governed by

$$\dot{\mathbf{q}}(\mathbf{x}, t) + \mathcal{L}\mathbf{q}(\mathbf{x}, t) = \mathbf{f}(\mathbf{x}, t), \quad (2.1)$$

where \mathbf{q} denotes the state of the system with respect to a reference state \mathbf{q}_0 , \mathcal{L} is a linear operator and \mathbf{f} represents an exogenous input or forcing. The space and time dimensions are denoted by \mathbf{x} and t , respectively. Assuming that the system is homogeneous in the temporal dimension, we propose solutions of the form (Schmid & Henningson 2001) $\mathbf{q}(\mathbf{x}, t) = \hat{\mathbf{q}}(\mathbf{x}) \exp(-i\omega t)$ with $\omega \in \mathbb{C}$, and substituting in (2.1) gives

$$(-i\omega\mathbf{I} + \mathcal{L})\hat{\mathbf{q}}(\mathbf{x}) = \hat{\mathbf{f}}(\mathbf{x}). \quad (2.2)$$

In the case there the forcing term is nonzero, the elements can be rearranged so that the governing equation represents the following system

$$\hat{\mathbf{q}}(\mathbf{x}) = (-i\omega\mathbf{I} + \mathcal{L})^{-1} \hat{\mathbf{f}}(\mathbf{x}) := \mathcal{H}_\omega \hat{\mathbf{f}}(\mathbf{x}). \quad (2.3)$$

We refer to \mathcal{H}_ω as the resolvent operator. Note that the subscript ω is retained to highlight the dependence on the temporal frequency. The original dynamical system in (2.1) has been recast as a linear mapping between a forcing $\hat{\mathbf{f}}$ and the state $\hat{\mathbf{q}}$.

According to (2.3), the properties of the state $\hat{\mathbf{q}}$ will be affected by both the nature of the forcing $\hat{\mathbf{f}}$ and the properties of the resolvent \mathcal{H}_ω . In this work, we focus in particular on the pairs of forcing-response that produce the largest amplification through the action of \mathcal{H}_ω . That is, a forcing of small magnitude yields a response of large magnitude. Such structures can be identified via a singular value decomposition (SVD) of the resolvent operator \mathcal{H}_ω as follows

$$\mathcal{H}_\omega = \sum_{j=1}^N \psi_j \sigma_j \phi_j^*, \quad (2.4)$$

where $\sigma_j \geq \sigma_{j+1} \geq 0$ for all j , and $(\cdot)^*$ denotes the adjoint. Notice that here the resolvent operator will take the form of a discretised operator, therefore the summation in (2.4) is truncated to N terms.

In particular, we seek $\hat{\mathbf{f}} = \phi_1$ that maximises the largest singular value σ_1 , where

$$\sigma_1 = \max_{\phi} \frac{\|\mathcal{H}_\omega \phi\|_2}{\|\phi\|_2} = \min_{\psi} \frac{\|\psi\|_2}{\|\mathcal{H}_\omega^* \psi\|_2}, \quad (2.5)$$

where the l_2 norm is taken over the spatial domain Ω_x , so that, for example,

$$\|\psi(\mathbf{x})\|_2 = \left(\int_{\mathbf{x} \in \Omega_x} |\psi(\mathbf{x})|^2 d\mathbf{x} \right)^{1/2}. \quad (2.6)$$

Alternatively, we can write this optimisation problem in terms of the leading forcing mode ϕ_1 as

$$\phi_1 = \arg \max_{\phi} \frac{\|\mathcal{H}_\omega \phi\|_2}{\|\phi\|_2}, \quad (2.7)$$

or the leading response mode ψ_1

$$\psi_1 = \arg \min_{\psi} \frac{\|\psi\|_2}{\|\mathcal{H}_\omega^* \psi\|_2}. \quad (2.8)$$

2.2. Resolvent formulation of the mean-linearised incompressible Navier–Stokes equations

The incompressible Navier–Stokes equations enforce conservation of momentum and mass, respectively, and are written in a Cartesian coordinate system as follows

$$\partial_t \mathbf{u} = -\mathbf{u} \cdot \nabla \mathbf{u} - \nabla p + \frac{1}{Re} \Delta \mathbf{u}, \quad (2.9)$$

$$\nabla \cdot \mathbf{u} = 0. \quad (2.10)$$

Here, the instantaneous velocity field has three components: $\mathbf{u} = [u(\mathbf{x}, t), v(\mathbf{x}, t), w(\mathbf{x}, t)]^T$ with $\mathbf{x} = [x, y, z]^T$ and $p = p(\mathbf{x}, t)$ represents the instantaneous pressure field. In this reference frame, x and z correspond to the streamwise and spanwise directions, respectively, and are nominally considered to be infinite in extent. The other variable, y , represents the wall-normal dimension. Here ∂_t denotes a time (partial) derivative, the spatial gradient operator is given by $\nabla = [\partial_x, \partial_y, \partial_z]^T$, and the Laplacian operator is defined as $\Delta = \nabla \cdot \nabla$.

We can write a given instantaneous velocity state \mathbf{u} as the sum of the temporal mean \mathbf{U} and a fluctuating component \mathbf{u}' , such that

$$\mathbf{u}(\mathbf{x}, t) = \mathbf{U}(\mathbf{x}) + \mathbf{u}'(\mathbf{x}, t). \quad (2.11)$$

Applying this decomposition in (2.9)–(2.10) and subtracting the temporal average gives the governing equations used in this work,

$$\partial_t \mathbf{u}' + \mathbf{U} \cdot \nabla \mathbf{u}' + \mathbf{u}' \cdot \nabla \mathbf{U} + \nabla p' - \frac{1}{Re} \Delta \mathbf{u}' = -\mathbf{u}' \cdot \nabla \mathbf{u}' - \overline{\mathbf{u}' \cdot \nabla \mathbf{u}'} = \mathbf{f}', \quad (2.12)$$

$$\nabla \cdot \mathbf{u}' = 0, \quad (2.13)$$

that is, conservation of momentum and continuity of the fluctuating components. Notice that here the right-hand side of (2.12) has been condensed into a forcing term \mathbf{f}' that represents the effect of the fluctuations about the mean state of the nonlinear terms, and can be regarded in this context as an exogenous input to a linear system comprising of the remaining terms. Wall-bounded parallel flows with a mean/base flow in the streamwise and spanwise dimensions $\mathbf{U}(y) = [U(y), 0, W(y)]^T$, admit a transformation of variables from a primitive reference $\{u', v', w', p'\}$ towards a reference in terms of the wall-normal velocity v' and vorticity η' (where $\eta' = \partial u' / \partial z - \partial w' / \partial x$), without loss of generality (i.e. resulting in the Orr–Sommerfeld and Squire equations). This formulation is proven to be equally informative (Moarref *et al.* 2013; Rosenberg & McKeon 2019; McMullen *et al.* 2020) for resolvent analysis of planar flows. In this reference, the no-slip and no-penetration conditions translate into $v'(y = 0) = v'(y = 2h) = 0$, $\partial_y v'(y = 0) = \partial_y v'(y = 2h) = 0$ and $\eta'(y = 0) = \eta'(y = 2h) = 0$, where h represents the semi-height of the domain in the wall-normal dimension. Throughout this paper, the location of the no-slip walls will coincide with $y = 0$ and $y = 2h$. This transformation is achieved according to the process described in Schmid & Henningson (2001), while including a spanwise component of the mean/base flow, W . The resulting wall-normal formulation of the conservation laws shown in (2.12)–(2.13) is formed by the following two equations

$$\left[(\partial_t + U \partial_x + W \partial_z) \nabla^2 - \partial_y^2 U \partial_x - \partial_y^2 W \partial_z - \frac{1}{Re} \nabla^4 \right] v' = f'_v, \quad (2.14)$$

$$\left(\partial_t + U \partial_x + W \partial_z - \frac{1}{Re} \nabla^2 \right) \eta' + (\partial_y U \partial_z - \partial_y W \partial_x) v' = f'_\eta. \quad (2.15)$$

Assuming that the system is homogeneous in the temporal dimension and the streamwise

and spanwise directions, we introduce assumed solutions of the form

$$v'(\mathbf{x}, t) = \hat{v}(y) \exp [i(k_x x + k_z z - \omega t)], \quad (2.16a)$$

$$\eta'(\mathbf{x}, t) = \hat{\eta}(y) \exp [i(k_x x + k_z z - \omega t)], \quad (2.16b)$$

$$\mathbf{f}'(\mathbf{x}, t) = \hat{\mathbf{f}}(y) \exp [i(k_x x + k_z z - \omega t)], \quad (2.16c)$$

where k_x and k_z denote the streamwise and spanwise wavenumbers, respectively, and ω denotes temporal frequency. Substituting these assumed solutions in (2.14)–(2.15) gives the following system of equations,

$$(-i\omega \mathbf{M} + \mathbf{L}) \begin{pmatrix} \hat{v} \\ \hat{\eta} \end{pmatrix} = \begin{pmatrix} \hat{f}_v \\ \hat{f}_\eta \end{pmatrix}, \quad (2.17)$$

where

$$\mathbf{M} = \begin{pmatrix} \hat{\Delta} & 0 \\ 0 & \mathbf{I} \end{pmatrix} \text{ and } \mathbf{L} = \begin{pmatrix} \mathcal{L}_{os} & 0 \\ ik_z \partial_y U - ik_x \partial_y W & \mathcal{L}_{sq} \end{pmatrix}. \quad (2.18)$$

The modified Laplacian operator $\hat{\Delta} = \partial_{yy} - (k_x^2 + k_z^2)$ is introduced for simplicity, and

$$\mathcal{L}_{os} = (ik_x U + ik_z W) \hat{\Delta} - \frac{1}{Re} \hat{\Delta}^2 - ik_x \partial_y^2 U - ik_z \partial_y^2 W, \quad (2.19)$$

$$\mathcal{L}_{sq} = ik_x U + ik_z W - \frac{1}{Re} \hat{\Delta}, \quad (2.20)$$

represent the Orr-Sommerfeld (OS) and Squire (SQ) operators, respectively. Premultiplying both sides of equation (2.17) by \mathbf{M}^{-1} and solving for the state $[\hat{v}(y), \hat{\eta}(y)]^T$ gives

$$\begin{pmatrix} \hat{v} \\ \hat{\eta} \end{pmatrix} = (-i\omega \mathbf{I} + \mathcal{L})^{-1} \begin{pmatrix} \hat{g}_v \\ \hat{g}_\eta \end{pmatrix} := \mathcal{H}_\omega \begin{pmatrix} \hat{g}_v \\ \hat{g}_\eta \end{pmatrix}, \quad (2.21)$$

where

$$\mathcal{L} = \mathbf{M}^{-1} \mathbf{L} \text{ and } \begin{pmatrix} \hat{g}_v \\ \hat{g}_\eta \end{pmatrix} = \mathbf{M}^{-1} \begin{pmatrix} \hat{f}_v \\ \hat{f}_\eta \end{pmatrix}. \quad (2.22)$$

This transfer function \mathcal{H}_ω is denoted as the resolvent operator, in analogy to the definition introduced for a general linear system in (2.3) when $z = -i\omega$. Note that the resolvent operator is dependent on the triad $\{\omega, k_x, k_z\}$, but for the sake of readability this dependence is indicated by the subscript ω . Expanding the terms in accordance to the derivation described in Rosenberg & McKeon (2019) gives

$$\begin{pmatrix} \hat{v} \\ \hat{\eta} \end{pmatrix} = \mathcal{H}_\omega \begin{pmatrix} \hat{g}_v \\ \hat{g}_\eta \end{pmatrix} := \begin{pmatrix} \mathcal{H}_{vv} & 0 \\ -\mathcal{H}_{\eta\eta}(ik_z \partial_y U - ik_x \partial_y W) \mathcal{H}_{vv} & \mathcal{H}_{\eta\eta} \end{pmatrix} \begin{pmatrix} \hat{g}_v \\ \hat{g}_\eta \end{pmatrix}, \quad (2.23)$$

where the scalar operators are defined as

$$\mathcal{H}_{vv} = (-i\omega + \hat{\Delta}^{-1} \mathcal{L}_{os})^{-1}, \quad (2.24)$$

$$\mathcal{H}_{\eta\eta} = (-i\omega + \mathcal{L}_{sq})^{-1}. \quad (2.25)$$

Notice that the formulation in wall-normal variables enables the study of the dynamical properties of each of the variables independently. Nevertheless, it is possible to define a direct transformation of the resolvent operator, as well as the resolvent modes, from wall-normal velocity and vorticity $\{v, \eta\}$ to primitive velocity variables $\{u, v, w\}$ (and vice versa), according to the mapping that was introduced in Meseguer & Trefethen (2003) and further developed and applied in Jovanović & Bamieh (2005); McKeon & Sharma (2010);

Moarref *et al.* (2013); Sharma *et al.* (2017). The cited transformation recasts the response and forcing modes in primitive variables as follows

$$\Psi_{(u,v,w)} = \mathbf{C}\Psi_{(v,\eta)}, \quad (2.26)$$

and

$$\Phi_{(u,v,w)} = (\mathbf{M}^{-1}\mathbf{B})^{-1}\Phi_{(v,\eta)}. \quad (2.27)$$

Here

$$\mathbf{C} = \frac{1}{k_{\perp}^2} \begin{pmatrix} ik_x \partial_y & -ik_z \\ k_{\perp}^2 & 0 \\ ik_z \partial_y & ik_x \end{pmatrix}, \quad (2.28)$$

and

$$\mathbf{B} = \begin{pmatrix} -ik_x \partial_y & -(k_x^2 + k_z^2) & -ik_z \partial_y \\ ik_z & 0 & -ik_x \end{pmatrix}, \quad (2.29)$$

represent the input and output matrices, respectively.

2.3. Space-time resolvent analysis

Here, we present a form of resolvent analysis that is applicable to time-varying systems. This generalisation is achieved by limiting the assumed directions of homogeneity to the streamwise and spanwise spatial dimensions. Thus, in analogy to the trajectories presented in (2.16) we let the solutions take the following form

$$v'(\mathbf{x}, t) = \hat{v}(y, t) \exp [i(k_x x + k_z z)], \quad (2.30a)$$

$$\eta'(\mathbf{x}, t) = \hat{\eta}(y, t) \exp [i(k_x x + k_z z)], \quad (2.30b)$$

$$\mathbf{f}'(\mathbf{x}, t) = \hat{\mathbf{f}}(y, t) \exp [i(k_x x + k_z z)]. \quad (2.30c)$$

Notice the more general dependence of these trajectories on both y and t , allowing the solutions to adopt any sort of temporal function. Substituting these spatio-temporal solutions in the governing equations in wall-normal formulation in (2.14)–(2.15), and solving for the current state $[\hat{v}(y, t), \hat{\eta}(y, t)]^T$ provides the following definition of the space-time resolvent operator \mathcal{H}_t

$$\begin{pmatrix} \hat{v} \\ \hat{\eta} \end{pmatrix} = \mathcal{H}_t \begin{pmatrix} \hat{g}_v \\ \hat{g}_\eta \end{pmatrix} := \begin{pmatrix} \tilde{\mathcal{H}}_{vv} & 0 \\ -\tilde{\mathcal{H}}_{\eta\eta}(ik_z \partial_y U - ik_x \partial_y W) \tilde{\mathcal{H}}_{vv} & \tilde{\mathcal{H}}_{\eta\eta} \end{pmatrix} \begin{pmatrix} \hat{g}_v \\ \hat{g}_\eta \end{pmatrix}, \quad (2.31)$$

and the modified scalar operators are given by

$$\tilde{\mathcal{H}}_{vv} = (\mathbf{D}_t + \hat{\Delta}^{-1} \mathcal{L}_{os})^{-1}, \quad (2.32)$$

$$\tilde{\mathcal{H}}_{\eta\eta} = (\mathbf{D}_t + \mathcal{L}_{sq})^{-1}. \quad (2.33)$$

Here, \mathbf{D}_t represents a generalised discrete time-differentiation operator, and the subscript in \mathcal{H}_t represents the triad $\mathbf{t} = \{t, k_x, k_z\}$. Notice that definitions (2.32) and (2.33) have the symbol $(\tilde{\cdot})$ to emphasise on the temporal dependence and disambiguate from (2.24) and (2.25). As before, resolvent analysis proceeds by taking an SVD of the associated resolvent operator, \mathcal{H}_t . The leading resolvent forcing and response modes satisfy the same optimisation problems described in equations 2.5, 2.7-2.8, though now the norm is computed over both space and time, so that

$$\|\psi(\mathbf{x}, t)\|_2 = \left(\int_{t \in \Omega_t} \int_{\mathbf{x} \in \Omega_{\mathbf{x}}} |\psi(\mathbf{x}, t)|^2 d\mathbf{x} dt \right)^{1/2}, \quad (2.34)$$

where Ω_t denotes the temporal domain under consideration.

While the theory of this generalization of resolvent analysis is straightforward, it does come with a potential increase in the computational cost. Upon discretization, the size of the matrix representation of the resolvent operator is increased by a factor of the number of timesteps, N_t , in both the row and column dimensions with respect to the space-only resolvent operator defined in (2.21). For a case with where one spatial dimension (y) is discretised, this means that the total size is $(2N_y N_t \times 2N_y N_t)$ and each of the block-elements is $(N_y N_t \times N_y N_t)$, where N_y and N_t are the number of discretisation points in the space and time dimensions, respectively. Note that the space-only formulation is constituted by a resolvent operator of total size $(2N_y \times 2N_y)$ and with block-elements of size $(N_y \times N_y)$. This increase is due to the fact that each of the entries of the operator \mathbf{D}_t corresponds to a temporal instance of a given spatial location in the wall-normal axis. For the purposes of this study, however, this computational cost remains feasible.

Note that in order to disambiguate between the space-only modes and the space-time modes, the symbol $(\hat{\cdot})$ will be used to denote the space-only modes in §3.

2.4. Sparse resolvent analysis

The theory presented in §2.1 formulates the finding the leading resolvent modes and corresponding gain as an optimization problem (e.g. (2.5)) in terms of the spatial l_2 norm of forcing and response modes (defined in (2.6)). Similarly, the leading resolvent modes for the space-time resolvent formulation described in §2.3 is formulated using the norms computed over both the spatial and temporal domains (2.34).

Such optimization problems involving the l_2 norm are ubiquitous across a broad range of methods, and arise naturally for methods based on the SVD. However, it is possible to modify such optimization problems such that their solution has different characteristic features.

Here, we introduce a variant of resolvent analysis that seeks to achieve localisation or sparsity, while also desiring the large energy amplification levels that are obtained in the standard resolvent formulation. This is achieved by incorporation of the variant of sparse principal component analysis (PCA) described in Hein & Bühler (2010). Similar approaches are discussed in Jolliffe *et al.* (2003); Zou *et al.* (2006); Sigg & Buhmann (2008); Journée *et al.* (2010); Zou & Xue (2018).

Sparsity is promoted through the incorporation of an additional term in the form of the l_1 -norm, which produces the following minimization problem

$$\psi_1 = \arg \min_{\psi} \frac{(1 - \alpha) \|\psi\|_2 + \alpha \|\psi\|_1}{\|\mathcal{H}^* \psi\|_2}. \quad (2.35)$$

Here, the sparsity parameter $\alpha \in [0, 1]$ determines the number of nonzero elements in ψ_1 . Moreover, the sparsest solution will be retrieved when $\alpha = 1$; while the case where $\alpha = 0$ will give the least sparse outcome and will in fact match the result given by (2.5).

Notice that the numerator in (2.35) is a convex function. The solution to this optimisation problem is achieved by reformulating it as a nonlinear eigenproblem that enables the use of an inverse power method to find its optimum (Hein & Bühler 2010). In practice, this method often produces solutions with sharp gradients, where some of the entries change drastically from zero to nonzero values. In order to produce coherent structures that resemble observable mechanisms, these solutions are regularised using the resolvent operator while maintaining sparsity. Here, we refer to the response modes computed on the first step as “raw” modes, and use a superscript to disambiguate from the regularised or updated modes. The full collection of steps that produces the sparse leading forcing ϕ_1 and response ψ_1 resolvent modes are described in algorithm 1.

The forcing modes could potentially be updated by substituting the updated response modes

Algorithm 1 Simplified sparse resolvent analysis

Input: Resolvent operator \mathcal{H} and sparsity parameter α

- 1: Compute raw sparse response modes ψ_1^{raw} by solving (2.35)
- 2: Compute corresponding forcing modes via

$$\phi_1 = \frac{\mathcal{H}^* \psi_1^{raw}}{\|\mathcal{H}^* \psi_1^{raw}\|_2} \quad (2.36)$$

- 3: Compute updated (regularised) response modes ψ_1 via

$$\psi_1 = \frac{\mathcal{H}\phi_1}{\|\mathcal{H}\phi_1\|_2} \quad (2.37)$$

- 4: Compute corresponding singular values via

$$\sigma_1 = \|\mathcal{H}\phi_1\|_2 \quad (2.38)$$

Output: Regularised sparse response mode ψ_1 , sparse forcing mode ϕ_1 , singular value σ_1 .

in (2.36), although in practice there is not a significant difference between the updated and the first forcing modes. In addition, it is possible to compute higher-order resolvent modes within this framework using the deflation scheme described in Bühler (2014). According to this, the components that have already been identified are removed from the optimisation space before following the steps presented above. Moreover, observe that the method described here promotes sparsity on the response modes ψ , although exchanging ψ with ϕ and \mathcal{H} with \mathcal{H}^* would yield sparsity-promotion in the forcing modes. Lastly, the subscript in the resolvent operator was removed in this section in order to indicate that this methodology can be applied to both the spatial and space-time resolvent operators. For an explicit and expanded form of this algorithm describing how the solution to (2.35) is obtained, refer to appendix A.

3. Results

In this section, we present the application of the proposed framework on four different systems. After describing numerical details associated with the resolvent calculations in §3.1, in §3.2 we showcase the implementation of sparse resolvent analysis on a statistically-stationary turbulent channel flow. Here, we consider conventional resolvent analysis with a Fourier transform in time, but enable sparsity promotion in the spanwise direction. We then consider the space-time resolvent operator for this problem in §3.3, and show that the proposed method can produce temporally-localised modes for a statistically stationary flow. We next apply sparse and non-sparse space-time resolvent analysis to two non-statistically-stationary systems, a periodic turbulent Stokes boundary layer in §3.4, and a turbulent channel flow with sudden lateral pressure gradient in §3.5.

3.1. Numerical methods

The mean velocity profiles used for resolvent analysis are all obtained from direct numerical simulations (DNS). These simulations use a staggered second-order finite difference scheme (Orlandi 2000), with a fractional step method (Kim & Moin 1985) and third-order Runge-Kutta time-advancing scheme (Wray 1990). Further details regarding the use and validations

of these methods, and their application to the specific cases considered here, can be found in Bae *et al.* (2018, 2019); Lozano-Durán & Bae (2019).

For resolvent analysis, the wall-normal direction is discretised using a Chebyshev collocation method. In the cases where the spanwise dimension is explicitly discretised, we use a Fourier discretisation scheme with periodic boundary conditions along the spanwise domain. Moreover, if homogeneity is not assumed in the temporal dimension, we adopt a Fourier discretisation scheme when the system is assumed to be statistically-stationary or time-periodic (i.e. §3.2–§3.4), and an explicit Euler finite-differentiation scheme in the temporal dimension with Neumann boundary conditions at the boundaries in §3.5. The corresponding differentiation operators for both Chebyshev and Fourier discretisations are defined according to the specifications given in Weideman & Reddy (2000). The number of collocation points used for each of the examples considered in this work will be indicated in the corresponding section. In each case, we verify that the numerical resolution gives converged results, with details of these convergence studies given in appendix B.

In the space-time implementations of the analysis showcased in this paper (i.e. §3.3–§3.5), no-slip and no-penetration conditions are enforced at $y = 0$ (lower wall), while free-slip and no-penetration conditions are enforced at $y = h$ (the channel centerline). The space-time analysis identifies modes that are sufficiently localised away from the mid-plane using the chosen set of parameters, allowing us to reduce the size of the numerical domain to the area below $y/h = 1$.

3.2. Spatially-sparse resolvent analysis of turbulent channel flow

Here, we apply the sparse resolvent analysis methodology on a fully-developed turbulent channel flow, where we consider spatial (rather than temporal) sparsity. The mean velocity profile is obtained from direct numerical simulations at a friction Reynolds number of $Re_\tau = 186$, defined as $Re_\tau = u_\tau h/\nu$ and the friction velocity, expressed as $u_\tau = \sqrt{\tau_w/\rho}$. The shear stress at the wall-boundary is denoted as τ_w , and h is the channel half-height. Hereafter, the superscript $(\cdot)^+$ denotes viscous (inner) units. In this reference, the velocities are scaled by the friction velocity u_τ , and the lengthscale is given by ν/u_τ . In order to showcase the application of the sparse formulation of resolvent analysis introduced in §2.4, we consider two configurations, both of which assuming homogeneity in the streamwise direction and the temporal dimension: a first case where the spanwise dimension is assumed to have an infinite extent, followed by a second implementation in which the spanwise dimension is limited to a finite periodic domain.

The first configuration represents a one-dimensional analysis, where the chosen wavelengths in the streamwise $\lambda_x^+ = 1000$ and spanwise $\lambda_z^+ = 100$ directions correspond to the average size of the streaks and vortices that arise in the near-wall cycle (Jiménez & Pinelli 1999). The temporal frequency is fixed at $\omega = 17.14$, where the temporal scale is normalised by the friction velocity, u_τ , and the half-height of the channel, h . In this application, the number of collocation points in the wall-normal direction is $N_y = 201$. No-slip and no-penetration conditions are enforced for the velocity at the upper and lower boundaries.

Results obtained from applying both standard and sparsity-promoting (in the wall-normal direction) resolvent analysis are shown in figure 1, where we show the amplitude of the streamwise velocity component of the leading two resolvent response modes. For standard resolvent analysis, the chosen wavenumbers and frequency produces modes with two peaks, each centered near one of the two critical layer locations (where $U(y) = \omega/k_x$). The leading two singular values are essentially identical, and represent the fact that the two peaks are separated from each other, and can each represent structures that have an arbitrary phase shift between them. Mathematically, these modes are basis vectors for a subspace of dimension

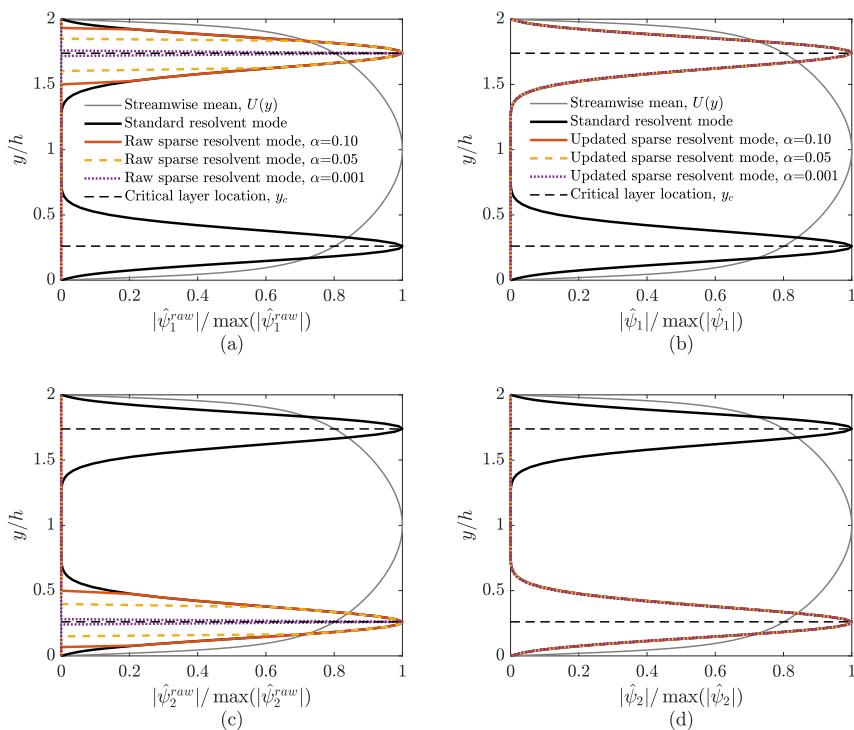


Figure 1: Streamwise components (u) of the first (a,b) and second (c,d) standard and sparse resolvent response modes computed for a turbulent channel flow with $Re_\tau = 186$, $\lambda_x^+ = 1000$, $\lambda_z^+ = 100$ and temporal frequency $\omega = 17.14$. Note that the standard modes (black) have been computed using (2.8), while (2.35) produced the raw sparse modes $\hat{\psi}^{raw}$ (a,c) from which we extract the adjusted modes $\hat{\psi}$ (b,d). The streamwise mean flow U is added to all plots for reference. The black dashed lines denote critical layer locations.

two, and thus an equally valid choice of basis for this subspace would be given by localised modes with one peak each.

To compare to the results of sparse resolvent analysis, several solutions are computed for different sparsity parameters α via the optimisation problem posed in (2.35). The obtained raw sparse resolvent modes are shown in figures 1(a) and 1(c) seem to be highly dependant on the corresponding value of α , although they are again all located near one of the two critical layer locations. This dependence on the sparsity parameter subsides after regularizing the modes following algorithm 1, as shown in figures 1(b) and 1(d). We observe that these regularized modes each recover one of the two peaks identified by regular resolvent analysis, indicating that the sparse variant is finding basis elements for the leading resolvent subspace that are spatially sparse. The sparse singular values (computed via (2.38)) are also consistent with the standard resolvent case, with σ_1 being about 1% lower for the sparse case (with $\alpha = 0.1$) in comparison with the non-sparse equivalent.

As the regularisation step appears to both remove the dependence on the sparsity parameter, and recovers the results for regular resolvent analysis for this example, we will exclusively use this regularised version for the remaining cases.

We now consider the same turbulent channel flow, but instead of assuming a Fourier decomposition in the spanwise direction, we instead explicitly discretise this dimension,

applying periodic boundary conditions with a spanwise extent twice the channel height. We use a Fourier basis in this spanwise dimension, with $N_z = 96$ collocation points (with $N_y = 201$ as before). Figure 2 shows the leading resolvent forcing and response modes obtained from standard and sparse resolvent analyses, visualised in the $y-z$ plane. Since the system is homogeneous in the spanwise dimension, the standard resolvent modes (figure 2(a,c)) give Fourier modes in this direction. The response mode consists of alternating slow- and fast-moving streamwise streaks, with streamwise vortices located between each streak. These streamwise streaks and vortices, centered at the critical layer, are consistent with typical structures observed in the near-wall cycle (Jiménez & Pinelli 1999). The wall-normal profile of these modes is close to matching those from the one-dimensional analysis shown in figure 1, where the identified spanwise wavelength for the leading mode is slightly different from that selected in the one-dimensional analysis shown in figure 1. The configuration of these streamwise streaks is consistent with the lift-up mechanism (Landahl 1975, 1980), through which streamwise vortices lead to the formation of streamwise streaks by transporting slow-moving fluid away from the wall, and vice-versa.

The sparse resolvent modes shown in figure 2(b,d) contain a spatially-localised unit of the periodic structures identified by standard resolvent in figure 2(a,c). In particular, the sparse response mode consists of a primary central vortex surrounded by a fast and slow streak, flanked by lower-amplitude secondary vortices and streaks. Note that while we are only showing the lower half of the domain, on the upper half the same structure is present for standard resolvent, but not for the sparse equivalent (again consistent with figure 1). While not shown here, higher-order sparse resolvent modes consist of repetitions of this localized structure both on the upper wall, and translated in the spanwise direction (with the spanwise location of the leading mode being arbitrary). Note also that the relative phase of the forcing and response modes is consistent between the regular and sparse modes.

Here the localised structure identified by sparse resolvent analysis can be interpreted as a “minimal” unit corresponding to similar linear energy amplification as standard resolvent analysis (with very similar singular values). In fact, this minimal unit identified by sparse resolvent analysis is reminiscent of instantaneous (Hutchins & Marusic 2007; Jiménez 2018) and conditionally-averaged (Dennis & Nickels 2011) structures and correlations (Sillero *et al.* 2014) that are observed in a turbulent flow field, suggesting the utility of this analysis for representing localised features and mechanisms within turbulent flows. In terms of the energy content of these structures, the first non-sparse singular value is about 1.003 times larger than its sparse counterpart.

3.3. Space-time resolvent analysis of a turbulent channel flow

In this section, we demonstrate the implementation of the non-sparse and sparse space-time variants of resolvent analysis on the statistically-stationary turbulent channel flow considered in §3.2. Here, we do not perform a Fourier transform in the temporal dimension, and instead implement the space-time formulation of resolvent analysis introduced in (2.31). All the parameters adopted in the analysis conducted in §3.2 are also adopted here (except for the frequency, which is no longer specified), and time is nondimensionalised by the friction velocity, u_τ , and the half-height of the channel, h .

First, the streamwise (u) and wall-normal velocity (v) components of the resolvent modes obtained from the non-sparse space-time analysis are shown in figure 3 with a time horizon $\tau_{tot} = 20\tau$ that spans over 20 cycles of length $\tau = 2\pi/\omega = 0.3659$, where $\omega = 17.14$ is the same frequency used in §3.2-3.3. The number of collocation points is $N_y = 101$ in the wall-normal direction and $N_t = 551$ in the temporal dimension.

As expected, we observe that the leading spacetime resolvent mode are Fourier modes in

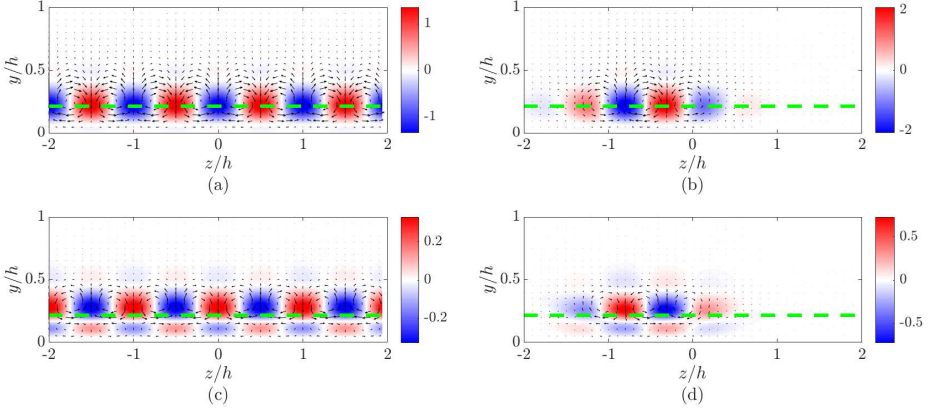


Figure 2: Real component of leading response modes $\hat{\psi}_1$ (a-b) and forcing modes $\hat{\phi}_1$ (c-d), for standard (a,c) and sparse (b,d) resolvent analysis, applied to turbulent channel flow at $Re_\tau = 186$, with a finite periodic domain in the spanwise direction defined by $z/h \in \{-2, 2\}$ and a frequency $\omega = 17.14$. Contours of streamwise velocity are shown, with arrows indicating the velocity in the spanwise (z) and wall-normal (y) directions. Green dashed lines indicate critical layer locations. The streamwise wavelength is $\lambda_x^+ = 1000$.

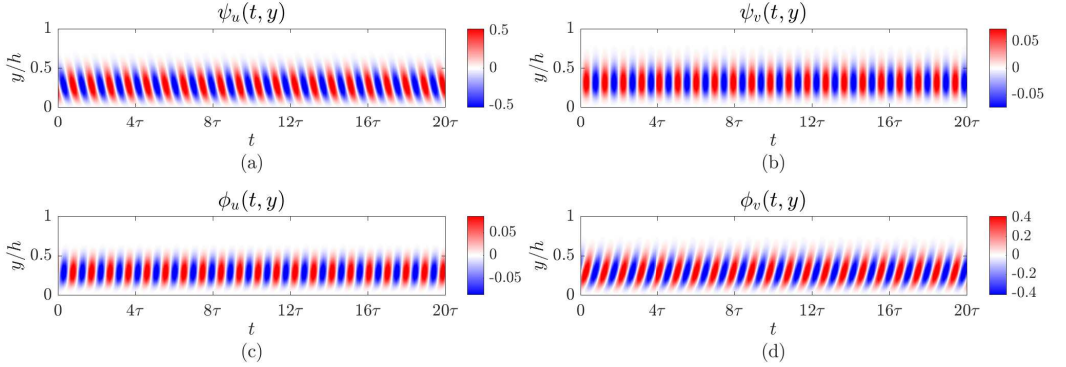


Figure 3: Real component of space-time leading response ψ_1 (a-b) and forcing ϕ_1 (c-d) modes of the resolvent operator in a turbulent channel flow with $Re_\tau = 186$, and $\lambda_x^+ = 1000$, $\lambda_z^+ = 100$ for a time horizon $\tau_{tot} = 20\tau = 20(2\pi/\omega)$. Subplots (a,c) show the streamwise velocity component (u), while (b,d) give the wall-normal component (v).

time, with a frequency that matches that used in the previous analyses (i.e. the mode exhibits twenty periods over the time domain of length 20τ).

To further demonstrate that the spacetime variant gives equivalent results to standard resolvent analysis, in figure 4 we compare the leading 30 singular values from both versions, where in the standard resolvent analysis we compile the results across all frequencies that are permissible when using this temporal domain (i.e. $\omega = 2\pi n/\tau_{tot}$ with $n \in \mathbb{Z}$).

We now consider the spatio-temporally sparse variant of this analysis. The total time horizon is again set to $\tau_{tot} = 20\tau$, which allows for the potential growth and decay of temporally-localised modes without the influence of the periodic boundary conditions. $N_y =$

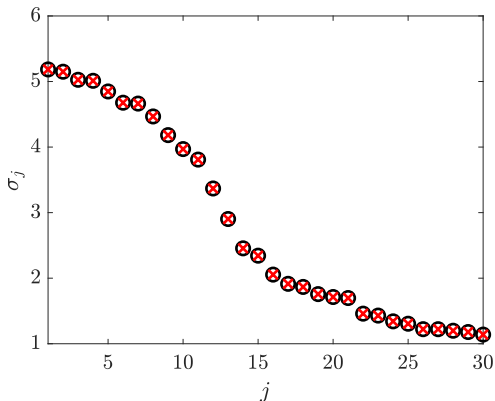


Figure 4: Leading 30 singular values of the space-time resolvent (black) and singular values of the space (standard) resolvent computed at $\omega_n = n(2\pi/\tau_{tot})$ with $-100 \leq n \leq 100$ sorted in descending order (red) for a turbulent channel flow with $Re_\tau = 186$, $\lambda_x^+ = 1000$, $\lambda_z^+ = 100$ with a time horizon (for the space-time variant) $\tau_{tot} = 20\tau = 20(2\pi/\omega)$, where $\omega = 17.14$.

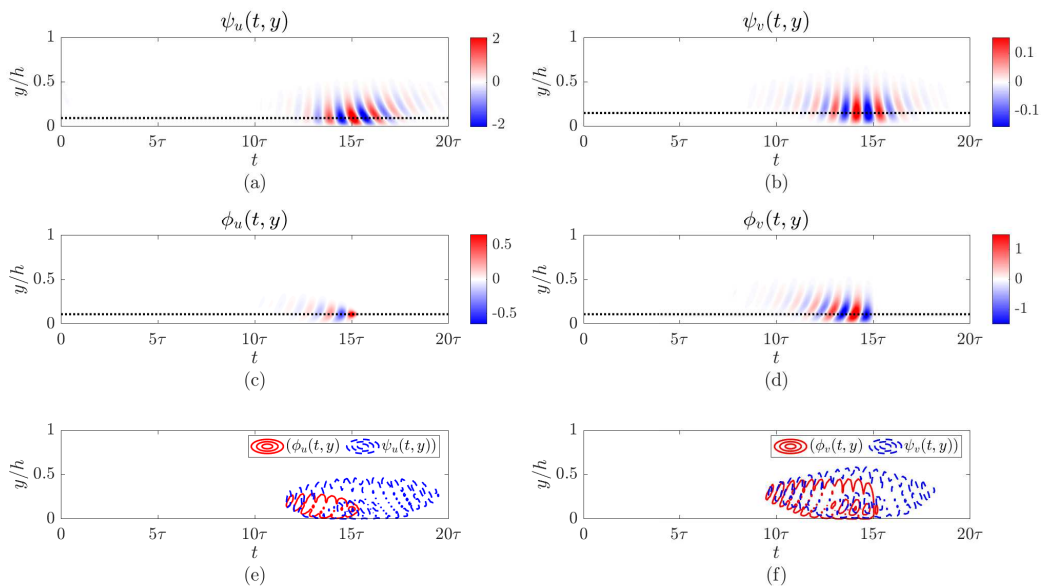


Figure 5: Real component of space-time sparse leading response ψ_1 (a,b) and forcing ϕ_1 (c,d) modes of the resolvent operator in a turbulent channel flow with $Re_\tau = 186$, and $\lambda_x^+ = 1000$, $\lambda_z^+ = 100$, computed with a sparsity parameter $\alpha = 0.001$, for a time horizon $\tau_{tot} = 20\tau = 20(2\pi/\omega)$. Horizontal dotted lines in (a-d) indicate the y -location where each mode component achieves its maximum amplitude. Subplots (e,f) show contour levels of the absolute value of leading forcing (red) and response (blue) modes.

101 collocation points are used in the wall-normal direction, and $N_t = 501$ in the time dimension. Figure 5 contains the streamwise and wall-normal components of the updated response and forcing modes with a sparsity parameter $\alpha = 0.001$. Notice how the analysis identifies structures that are sparse both in the spatial and temporal dimensions. As was the case for the spanwise channel discussed in §3.2, these modes depict a minimal linear

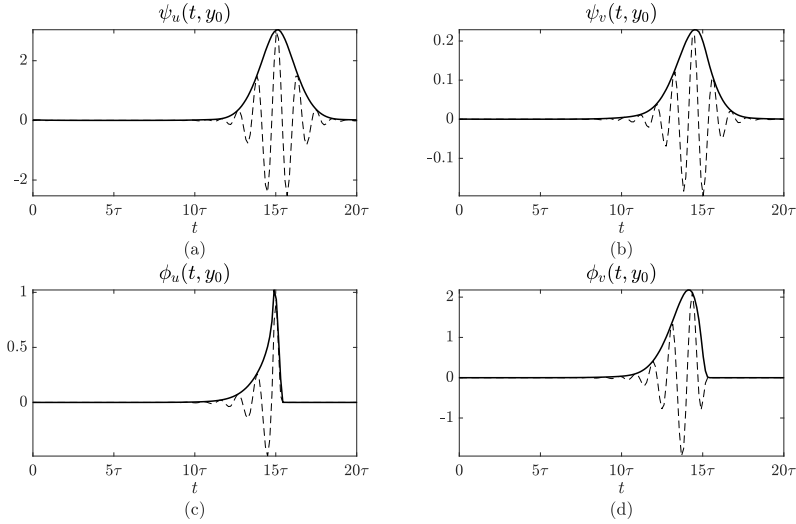


Figure 6: Absolute (solid) and real (dashed) components of the temporal evolution of the sparse modes shown in figure 5(a-d), at the y -locations of maximum amplitude.

amplification unit, in this case formed by a localised version of the modes identified by the non-sparse space-time analysis in figure 3. Observe that the forcing modes in figure 5(c,d) precede the response in figure 5(a,b). The phase variation in time (corresponding to the temporal frequency) and wall-normal location of the modes approximately match those identified from the leading non-sparse space-time resolvent mode shown in figure 3. The sparse mode, however, identifies aspects of the physics that cannot be directly observed without sparsity-promotion (and thus localisation), such as the change in inclination angle and wall-normal location of the mode components with time. In particular, the inclination angle of structures tend to lean further backwards in the $y-t$ plane as time increases, which would correspond to an increased downstream tilt over time in the $x-y$ plane, consistent with the Orr mechanism (Orr 1907).

We also note that these time-localized resolvent mode components indicate the causal mechanisms producing energy amplification, with forcing in v proceeding response in v (figure 5f) which in turn proceeds the (energetically-dominant) response in u (figure 5e), consistent with the lift-up mechanism. In terms of the energy content, for a fixed time horizon of 20τ , the leading non-sparse singular value is larger than the leading sparse one by a factor of 5.60.

To explore the temporal profiles of the components of these sparse space-time modes, figure 6 shows the cross-sections along the t -axis of the sparse modes in figure 5 at the locations in y where the amplitude of the signal finds its maximum. The temporal evolution of the forcing mode components seems to be more localised in these cross-sections, as they abruptly drop to zero near where the amplitude of the response modes finds its maximum value. The shape of the streamwise and wall-normal components of the modes (first row in figure 5) shows an approximately Gaussian envelope with approximately constant phase gradient, with a phase variation that is approximately uniform across all mode components. This could potentially suggest a natural choice of wavelet basis functions for a low order temporally-localised analysis of this flow (Ballouz *et al.* 2023, 2024). Moreover, the particular shape of the response modes could enable the implementation of wavepacket pseudomode

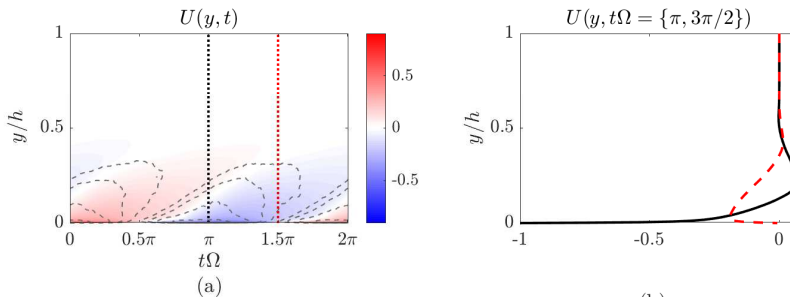


Figure 7: (a) Streamwise mean flow $U(y, t)$ (colourmap) and streamwise turbulence intensity u_{rms} (grey dashed) of a turbulent Stokes boundary layer, with levels indicating $\{20\%, 30\%, 50\%, 75\%, 95\%\}$ of its maximum value, over a full oscillating cycle; (b) time-instances of the turbulent mean at $t\Omega = \pi$ (black) and $t\Omega = 3\pi/2$ (red).

theory to approximate these response modes (Obrist & Schmid 2010, 2011; Mao & Sherwin 2011; Edstrand *et al.* 2018; Dawson & McKeon 2019, 2020).

3.4. Space-time resolvent analysis of a turbulent Stokes boundary layer

In this section, we apply non-sparse and sparse space-time resolvent analysis to a turbulent Stokes boundary layer, with a time-periodic mean velocity field as shown in figure 7). This flow sits between two plates that oscillate synchronously with a velocity given by

$$U_w(t) = U_0 \cos(\Omega t), \quad (3.1)$$

with U_w denoting the velocity of the oscillating walls and U_0 representing a constant. There is no external pressure gradient, so the flow is entirely driven by the motion of the walls. The Reynolds number for this flow is defined as a function of the frequency of the oscillations Ω , such that $Re_\Omega = U_0 \delta_\Omega / \nu$, and $\delta_\Omega = \sqrt{2\nu/\Omega}$ is a length parameter denoting the boundary layer thickness. For the ensuing analysis, we choose $Re_\Omega = 1500$ to ensure that the flow lies in the intermittently turbulent regime (Hino *et al.* 1976; Akhavan *et al.* 1991; Verzicco & Vittori 1996; Vittori & Verzicco 1998; Costamagna *et al.* 2003). Note that while there appears to be little prior work performing linear analyses of this configuration in the turbulent regime, linear analysis of laminar pulsatile channel flow has been considered using Floquet analysis (Pier & Schmid 2017) and optimally time-dependent modes (Kern *et al.* 2021).

The mean velocity profile and the root-mean-square (r.m.s.) of the fluctuating turbulent velocity components are obtained through direct numerical simulations as described in §3.1. The size of the domain for the DNS is $6\pi\delta_\Omega \times 80\delta_\Omega \times 3\pi\delta_\Omega$ (in the streamwise, wall-normal, and spanwise directions respectively) and contains 64, 385 and 64 grid points in each of the corresponding dimensions. To collect mean data, the DNS was run for 100 eddy turnover times after the decay of transient startup effects, where here we define this timescale as δ_Ω/u_τ , with $\delta_\Omega = 0.025h$. The time-periodic mean velocity profile is obtained through averaging in the dimensions of spatial homogeneity (i.e. the streamwise and spanwise directions), for each phase of wall motion. For resolvent analysis, the size of the numerical domain is $[0, h] \times [0, \tau_{tot}]$ with $h = 1$ and τ_{tot} being the length of the time horizon.

For performing both sparse and non-sparse space-time resolvent analysis, we consider wavelengths corresponding to the extent of the DNS computational domain, i.e. $\lambda_x = 6\pi\delta_\Omega \approx 0.471h$ and $\lambda_z = 3\pi\delta_\Omega \approx 0.236h$. That is, we look at the largest three-dimensional structure that the DNS would be capable of resolving. The reason for focusing on such large structures in x and z is that we expect that they will correspond to space-time resolvent modes that also

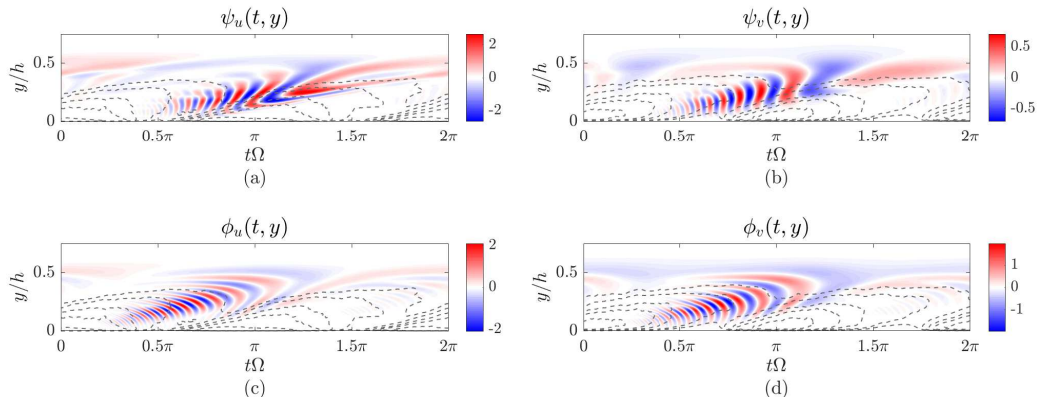


Figure 8: Real component of leading space-time resolvent (a,b) response ψ_1 and (c,d) forcing ϕ_1 modes of the resolvent operator in a turbulent Stokes boundary layer with $\lambda_x/h=0.471$ and $\lambda_z/h=0.236$ during a full oscillating cycle. The grey dashed lines represent the (a,c) streamwise and (b,d) wall-normal turbulence intensity, with contours at $\{15\%, 20\%, 30\%, 40\%, 60\%\}$ and $\{22\%, 30\%, 45\%, 55\%, 70\%\}$ of the maximum value of u_{rms} and v_{rms} , respectively.

have a large extent in t and y , allowing for the distinction between the sparse and non-sparse variants to be clearly observed.

For the non-sparse implementation of resolvent analysis, the domain is discretised using $N_y = 105$ collocation points in the wall-normal axis and $N_t = 651$ collocation points in the temporal dimension over a time window comprised of one oscillating cycle. The streamwise and wall-normal velocity components of the leading forcing and response modes obtained from this analysis are shown in figure 8, along with the corresponding streamwise and wall-normal turbulence intensity computed from the DNS. Observe that the identified coherent structures do not correspond to a single temporal Fourier mode. Instead, they are concentrated over approximately half of the full oscillation period. Although not shown here, the second leading resolvent mode depicts a coherent structure of almost identical energy content that is similar to the leading modes in figure 8, with a relative temporal shift of a half-period.

The location of the modes along the y -axis shifts away from the wall as the mean flow evolves over time. This angle in the $y-t$ plane appears to be similar to that observed for the turbulence intensities, suggesting that the mode depicts an energy transfer mechanism away from the wall that is present in the full nonlinear system. These modes are not concentrated in the near-wall region where the mean shear and turbulence intensity is largest. In this region, the turbulent energy content is likely dominated by structures at smaller lengthscales than the wavelengths considered here. We do observe, however, in figure 8(a) that the streamwise velocity response is amplified as the mode enters a region of higher streamwise turbulence intensity at $(t\Omega, y/h) \approx (\pi, 0.2)$.

Additionally, these modes depict structures with a time-varying characteristic frequency, with the frequency of oscillation decreasing over time as the structures move away from the wall and ultimately decay. This evolution of the frequency within a single space-time mode would not be directly captured via harmonic resolvent analysis, where each component mode is associated with a single temporal frequency (though triadic interactions between different frequencies could be isolated with this approach).

For the sparse implementation of space-time resolvent analysis at the same wavelengths, we adopt the same time horizon as in the non-sparse case, and a numerical domain with $N_y = 101$ collocation points in the wall-normal axis and $N_t = 631$ collocation points in the temporal dimension, with a sparsity parameter $\alpha = 0.001$.

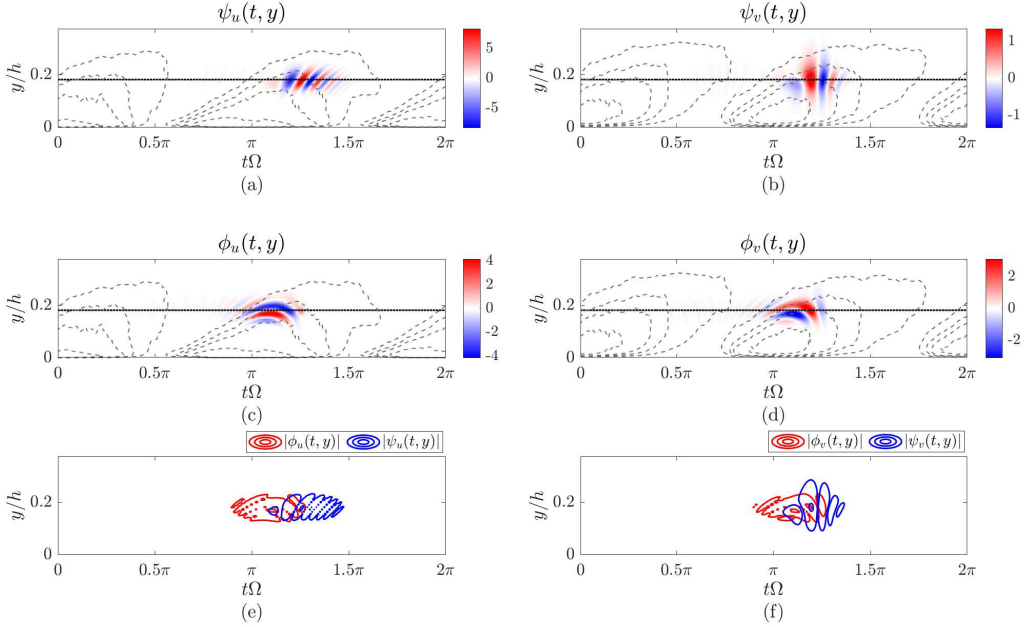


Figure 9: Real component of sparse space-time leading (*a,b*) response ψ_1 and (*c,d*) forcing ϕ_1 of the resolvent operator for a turbulent Stokes boundary layer with $\lambda_x/h=0.471$ and $\lambda_z/h=0.236$, computed with a sparsity parameter $\alpha = 0.001$, across a full oscillation cycle. Subplots (*e,f*) show contour levels of the absolute value of leading forcing (red) and response (blue) modes. The grey dashed lines represent the corresponding streamwise and wall-normal turbulence intensity, with contour levels at $\{23\%, 32\%, 40\%, 50\%, 70\%\}$ and $\{35\%, 45\%, 60\%, 75\%\}$ of the maximum value of u_{rms} and v_{rms} , respectively. The dotted lines correspond to the location in the y -axis where the amplitude of the modes finds its maximum value.

The leading sparse resolvent modes are shown in figure 9, again overlaid with contour levels of the streamwise and wall-normal turbulence intensity. We observe that at these streamwise and spanwise wavelengths, the structure of the leading resolvent modes differs substantially between the non-sparse and sparse analyses. In figure 9, the sparse analysis identifies localised structures for which the streamwise and wall-normal components are concentrated within one quarter of the total temporal domain, and within a small spatial region near $y/h = 0.2$ (note that the vertical range shown in figure 9 is smaller than in figure 8). Moreover, both forcing mode components precede their corresponding response modes (shown directly in figure 9(*e-f*)), with peak response in v preceding that for u , which was also observed in the sparse modes computed for statistically-stationary channel flow in §3.3. Comparing the sparse modes with the non-sparse counterparts in figure 8, the sparse analysis favours structures that are closer to the peak of the turbulence intensity.

Finally, figure 10 shows cross-section of these sparse modes along the temporal axis at the y -locations where they achieve their maximum amplitude (see the dotted lines indicated in figure 9). Comparing figures 5 and 10, we observe greater variation in the phase both within and across each mode component for the time-varying Stokes boundary layer configuration. For example, the streamwise velocity response in figure 10(*a*) shows that the rate of phase variation increases over time. The phase variation in the streamwise component of the sparse forcing mode is much slower, which figure 9(*c*) shows is due to the almost horizontal inclination of this component. As was the case in figure 5, we observe that the forcing mode

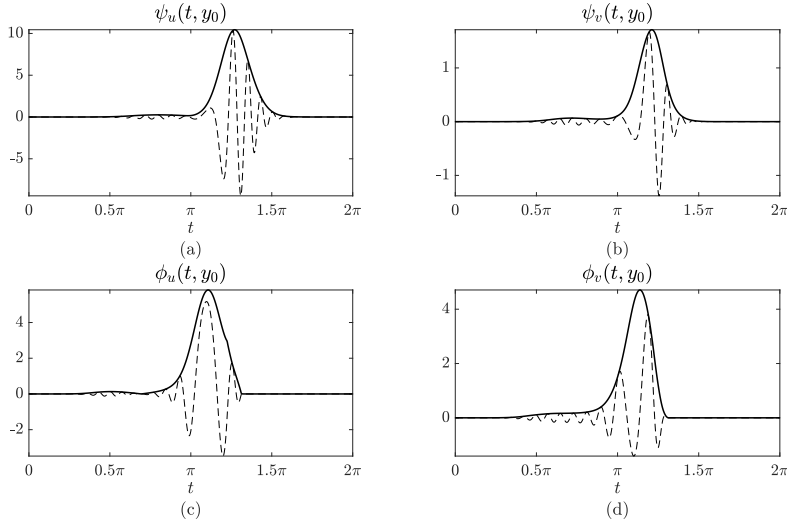


Figure 10: Absolute (solid) and real (dashed) components of the temporal evolution of the sparse modes shown in figure 9(a-d), at the y -locations of maximum amplitude.

components have envelopes that are less symmetric in time, abruptly decaying to zero at a given cutoff time.

3.5. Space-time resolvent analysis of a turbulent channel flow with sudden lateral pressure gradient

The last case considered in this work is a fully-developed turbulent channel flow at $Re_\tau = 186$ that is subjected to a sudden lateral pressure gradient at $t = 0$. The spanwise pressure gradient is related to the fixed streamwise gradient by $\partial p/\partial z = \Pi(\partial p/\partial x)$, where here we use $\Pi = 30$. Additional information about this configuration can be found in Moin *et al.* (1990); Lozano-Durán *et al.* (2020). The turbulent mean flow therefore contains both streamwise $U(y, t)$ and spanwise $W(y, t)$ nonzero components, which evolve over time until the system reaches its new statistically-stationary state. These velocity components are shown in figure 11.

To form the resolvent operator, the temporal domain is implicitly nondimensionalised by the initial friction velocity $u_{\tau,0}$ at $t = 0$, and h , and it is determined in two steps to achieve numerical accuracy. It is first defined as the interval $[-0.58, 2.34]h/u_\tau$ to extend the numerical domain before the initial condition to include time prior to the application of the spanwise pressure gradient. Thus, for $t < 0$ the base flow is constant, with $U(t < 0, y) = U(T = 0, y)$ and $W(t < 0, y) = 0$, and $\partial p/\partial z(t < 0) = 0$. After a first analysis is conducted, the time domain is restricted to a smaller temporal window near the observed temporal location of the leading modes that is large enough to produce unaltered results with a larger temporal resolution. Note that here we implement an explicit Euler finite-differentiation scheme in the temporal dimension. Thus, the final numerical domain used in this analysis is given by $[0, h] \times [0.4, 2]h/u_\tau$.

As was the case for statistically-stationary channel flow studied in §3.2-3.3, we concentrate our analysis on streamwise and spanwise wavenumbers corresponding to the typical size of near-wall streaks. After the pressure gradient is applied, the magnitude and direction of the mean flow changes, meaning that the wavelengths associated with near-wall streaks is also expected to change. Assuming that near-wall streaks adjust their size and orientation with

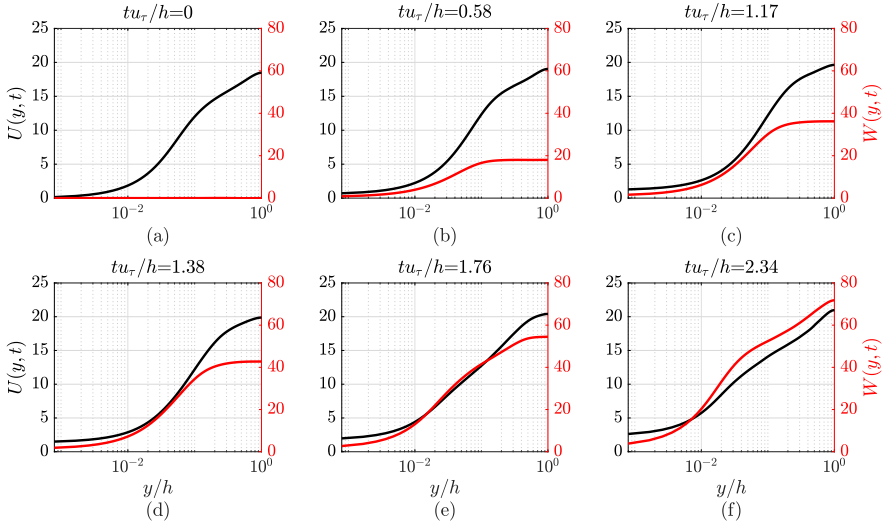


Figure 11: Temporal evolution of the streamwise $U(t, y)$ (black) and spanwise $W(t, y)$ (red) mean velocity profiles obtained by DNS of a turbulent channel flow at $Re_\tau = 186$ with sudden lateral pressure gradient at $t = 0$ with $\partial p/\partial z = \Pi(\partial p/\partial x)$ and $\Pi = 30$ at $tu_\tau/h \in \{0, 0.58, 1.17, 1.38, 1.76, 2.34\}$ (Lozano-Durán *et al.* 2020).

the mean, we can select wavelengths corresponding to the typical size of near-wall streaks at a certain point in time (Ballouz *et al.* 2024). Here, we select $\lambda_x^+ = 189$ and $\lambda_x^+ = 1890$, which correspond to the typical length of the near-wall streaks at a time instance $tu_\tau/h = 1.38$.

For the non-sparse space-time resolvent analysis, the domain is discretised using $N_y = 132$ and $N_t = 500$ collocation points. Leading resolvent mode components for this analysis are shown in figure 12. We observe that the modes are localised in time, centered near to the nominal time ($tu_\tau/h = 1.38$) where the scale of the modes coincides with near-wall streaks. The structure of the modes shares some similarities with those observed for both the non-sparse and sparse analyses of stationary channel flow (figures 3 and 5). In all cases, the wall-normal response consists of vertically-aligned structures, while the forcing is inclined upstream in the $y - t$ plane. The u -component of the response appears to incline further backwards as y progresses in both figures 5(a) and 12(a), though the later does appear to move towards and move away from the wall as observed in the former. Note that the u -component plotted in figure 12 no longer entirely corresponds to the streamwise direction, due to the spanwise pressure gradient.

Figure 12(e-f) show that the forcing and response mode components are all located over approximately the same time interval for this case. This is different from the sparse analysis of statistically-stationary channel flow (see figure 3(e-f)), where the forcing mode components decayed before their responses did, and the wall-normal forcing and response components started before the streamwise components. These differences can likely be attributed to the differences in how localised modes are obtained; for the 3D channel configuration we are not explicitly promoting sparse modes, but rather the modes are aligning with a region of time corresponding to a mean flow with maximum linear energy amplification for structures at the specified spatial scales. This can be further explored by applying the sparse variant to this configuration.

For the sparse implementation of space-time resolvent analysis, we adopt the same

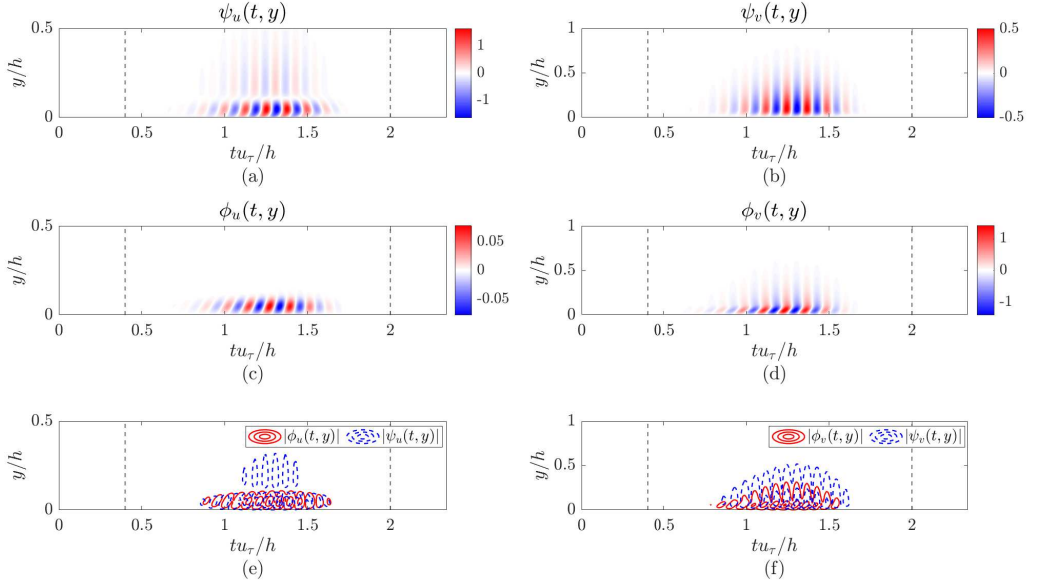


Figure 12: Real component of space-time u and v velocity components of the leading (a,b) response ψ_1 and (c,d) forcing ϕ_1 modes of the space-time resolvent operator for a channel flow with sudden lateral pressure gradient with $Re_\tau = 186$, and $\lambda_x^+ = 189$, $\lambda_z^+ = 1890$. (e,f) Contour levels of the absolute value of the leading forcing (red) and response (blue) modes. The dotted lines correspond to the location in the y -axis where the amplitude of the modes finds its maximum value. The grey dashed lines represent the boundaries of the temporal numerical domain.

wavelengths and a sparsity parameter $\alpha = 0.005$. The domain is discretised using $N_y = 130$ and $N_t = 500$ collocation points. The leading sparse modes are shown in figure 13, where both the u and v components display a similar structure, but with more temporal localisation, to those shown for the non-sparse analysis in figure 12.

The sparse analysis thus appears to identify the same mechanism, localised around the same region in time. Unlike the non-sparse version, here we observe in figure 13(e-f) differences in the temporal footprints of each mode component, with the decay in amplitude of the both components of the forcing preceding the decay of the response.

The cross-sections along the time axis of the modes contained in figures 12 and 13 are shown in figure 14 in red and black, respectively. The amplitudes of both the non-sparse and sparse modes adopt qualitatively similar envelopes, with the sparse variant being narrower, and centered at a slightly later time. We emphasise that unlike the profiles shown in figure 6, here the time-location of these modes is not arbitrary, and corresponds to a region of time where the mean profile enables the largest linear amplification. The phase variation is similar across all mode components, indicating a characteristic frequency maximising amplification. Here, we thus find that both sparse and non-sparse space-time resolvent appear to identify the same amplification mechanism, with the addition of the l_1 -norm term in the objective function restricting the sparse modes to a smaller temporal window.

Lastly, to demonstrate the numerical convergence of the results presented in this section, figure 15 presents the first ten singular values of the non-sparse and sparse with $\alpha \in \{0.005, 0.15\}$ space-time resolvent operators against the leading singular values obtained in the study described in Ballouz *et al.* (2024), where the numerical methods utilize a wavelet

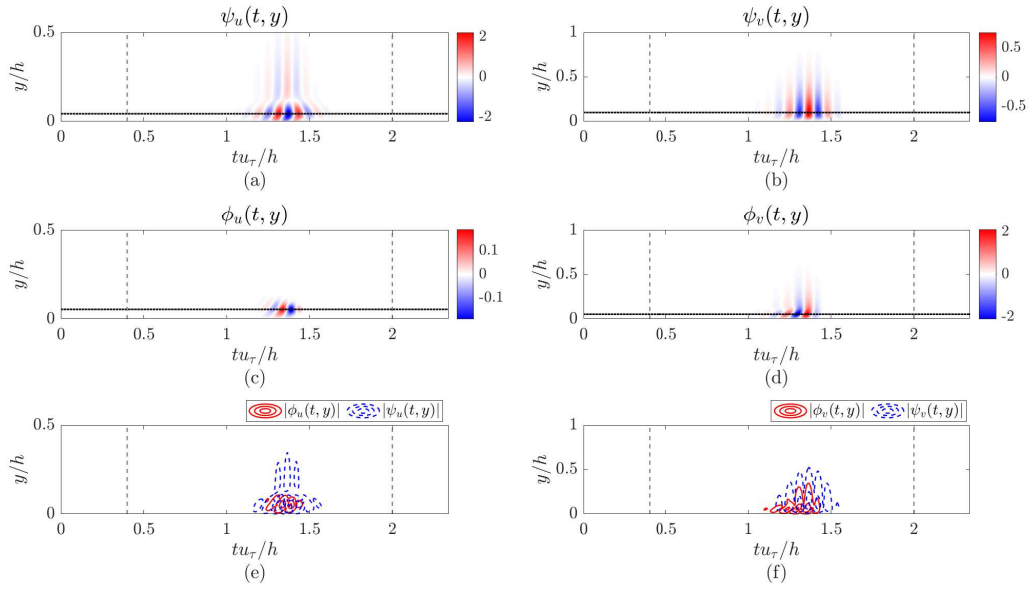


Figure 13: Real component of sparse space-time u and v velocity components of the leading (a,b) response ψ_1 and (c,d) forcing ϕ_1 modes of the space-time resolvent for a channel flow with sudden lateral pressure gradient with $Re_\tau = 186$, and $\lambda_x^+ = 189$, $\lambda_z^+ = 1890$ with a sparsity parameter $\alpha = 0.005$. (e,f) Contour levels of absolute value of the leading forcing (red) and response (blue) modes. The dotted lines correspond to the location in the y -axis where the amplitude of the modes finds its maximum value. The grey dashed lines represent the boundaries of the temporal numerical domain.

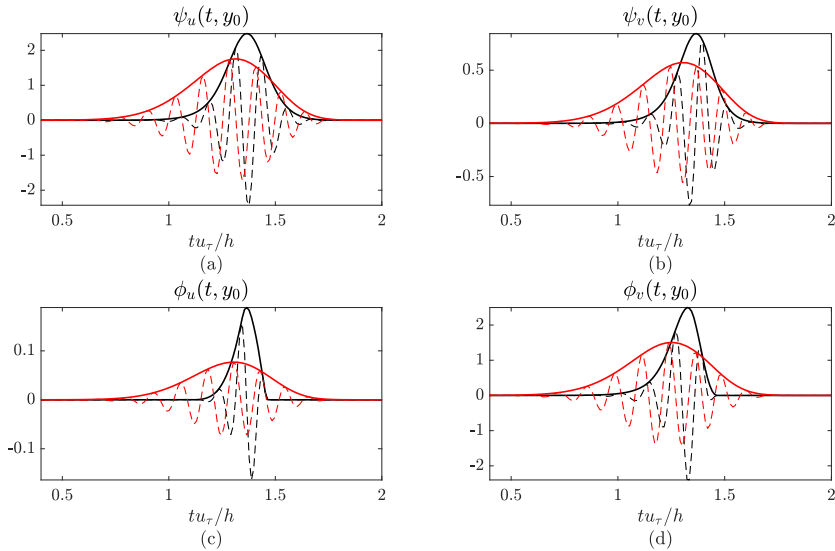


Figure 14: Absolute (solid) and real (dashed) components of the temporal evolution of the sparse modes shown in figure 12(a-d) (red) and figure 13(a-d) (black), at the y -locations of maximum amplitude.

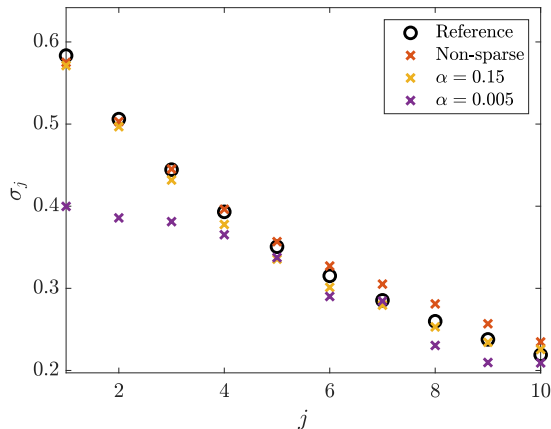


Figure 15: Leading 10 singular values of the nonsparse and sparse (with $\alpha \in \{0.005, 0.15\}$) space-time resolvent operator for a channel flow with sudden laterallateral pressure gradient with $Re_\tau = 186$, and $\lambda_x^+ = 189$, $\lambda_z^+ = 1890$. The reference values correspond to the analysis described in Ballouz *et al.* (2024).

transform in time. The corresponding leading modes coincide with figure 12 and figure 13 in the non-sparse and sparse (with $\alpha = 0.005$) implementation of the space-time analysis, respectively. First, observe that the singular values of the non-sparse analysis closely match the reference values. Second, a sparsity parameter of $\alpha = 0.15$ is sufficient large to obtain similar amplification levels to these reference values (note that the corresponding modes are not shown in this paper). This agreement also confirms the convergence of the sparse analysis. However, the singular values retrieved from the sparse analysis with $\alpha = 0.005$, retrieve only a portion of the reference values. In particular, the leading reference value is larger than the leading sparse singular value by a factor of 1.459, and we observe that this ratio decreases for higher-order singular values. The fact that the sparse and non-sparse analyses yield similar results for this case is likely due to the highly transient nature of the flow, where the leading resolvent modes are naturally localised even without explicitly promoting sparsity.

4. Discussion and Conclusions

In this work, we have proposed a sparse space-time variant of resolvent analysis that can identify time-localised coherent structures. These spatio-temporal structures correspond to the inputs and outputs that optimise an objective function that promotes large linear energy amplification, while also promoting the localisation in space and time of these structures. Localisation is achieved through the addition of a sparsity-promoting l_1 -norm term to the standard optimisation problem used for resolvent-type analyses. The new optimisation problem takes the form of a nonlinear eigenproblem, for which the optimal solution is achieved through an inverse power method.

We have demonstrated the implementation of this sparse variant of resolvent analysis on several different configurations, demonstrating that we obtain sparse modes first in the spatial domain, and also in the spatial and temporal domains when using a generalised space-time formulation of resolvent analysis. The first case studied was a statistically-stationary turbulent channel flow, a canonical configuration that has received substantial prior study in the context of resolvent analysis (and for many other forms of analysis). When using the standard Fourier transform in time, the proposed sparse resolvent analysis identified spatially-sparse modes, in

either the wall-normal or wall-normal and spanwise dimensions, depending on the problem setup. This provides a means for identifying localised spatial structures corresponding to similar amplification as the non-localised structures identified in standard resolvent analysis.

Next, a space-time generalisation of resolvent analysis was applied to the same channel flow configuration. Being a statistically-stationary system, each of the space-time modes converged to a single temporal Fourier mode, in the absence of sparsity-promotion. Therefore, the space-time resolvent modes are equivalent to the standard resolvent modes compiled across all frequencies permissible by the prescribed time horizon. The sparsity-promoting variant of this space-time resolvent analysis yielded structures that displayed localisation in both the spatial and temporal dimensions. These modes again reflect the fact that linear energy amplification can arise from forcing that is limited to a localised region in time. These time-localised structures can exhibit features that cannot be seen in Fourier modes, such as the inclination angles and wall-normal locations of structures evolving over time. Future work could quantitatively explore the extent to which these modes predict phenomena present in turbulent channel flow data.

Beyond statistically-stationary systems, we next explored the application of our proposed methodology to systems with a time-varying mean. The first such system that was considered was a time-periodic turbulent Stokes boundary layer. In this case, the non-sparse and sparse variants identified leading resolvent modes that were qualitatively different, with the sparse models being significantly more localised in both space and time. Our analysis focused on relatively large-scale structures by specifying streamwise and spanwise wavelengths corresponding to the size of the domain used for DNS. While not shown here, we found that this difference is less apparent for smaller wavelengths, where even the non-sparse variant identified structures that were localised in time, such as the case considered in Ballouz *et al.* (2024). For the case considered here, the sparse mode components identified were also localised near the peak in turbulence intensity at the wall-normal location where they were situated, suggesting that they identify a mechanism relevant to the generation and amplification of turbulent features at this temporal phase of the system.

The final set of results considered a non-periodic, time-evolving turbulent channel flow subjected to a sudden lateral pressure gradient. This flow was studied during a temporal window in which the flow transitions between two statistically-stationary states. It was found that both the non-sparse and sparse modes showed temporal localisation, presumably due to the choice of wavelengths permitting largest energy amplification in a certain time window corresponding to a given orientation of the mean. Overall, we have demonstrated that spatio-temporally sparse resolvent analysis can identify features that can either be qualitatively similar or distinct from the non-sparse equivalent.

The focus of this work has been the development and demonstration of this method across a range of flow configurations. Additional investigations into each of these (and other) configurations are required to quantify the extent to which these methods can be used to predict and understand structures and statistics of such turbulent flows, over a wider range of spatial scales. The numerical methods employed in the present work have required the explicit formation and decomposition of linear operators discretised in both space and time. Future work could also investigate timestepping approaches to perform such analyses. Such methods, which have been applied for resolvent (Martini *et al.* 2020; Farghadan *et al.* 2023) and other linear analyses (Barkley *et al.* 2008), would likely be particularly computationally-advantageous for our methodology.

Acknowledgements

This work was supported by the Air Force Office of Scientific Research grant FA9550-22-1-0109 and National Science Foundation Award number 2238770. The authors gratefully acknowledge the advanced computing resources made available through ACCESS project MCH230005.

Declaration of Interests

The authors report no conflict of interest.

Appendix A. Notes on the inverse power method for nonlinear eigenproblem used in sparse resolvent analysis

This appendix contains a detailed description of the inverse power method proposed by Hein & Bühler (2010) that is employed to solve the constrained optimisation problem posed by the sparse PCA algorithm, adapted to perform sparse resolvent analysis in §2.4. We start by considering a general nonlinear eigenproblem of the form

$$r(\mathbf{f}) - \lambda s(\mathbf{f}) = 0, \quad (\text{A } 1)$$

where \mathbf{f} represents the eigenfunction associated to the eigenvalue λ , and r and s are nonlinear operators. In order for \mathbf{f} to be a solution to the nonlinear eigenproblem, \mathbf{f} has to be a critical point of a functional, F . In this problem, the functional F is expressed as

$$F(\mathbf{f}) = \frac{R(\mathbf{f})}{S(\mathbf{f})}, \quad (\text{A } 2)$$

where both S and R represent convex, non-negative, Lipschitz continuous functionals that satisfy the positive homogeneity property $R(\gamma\mathbf{f}) = \gamma R(\mathbf{f})$ for $\gamma \geq 0$. The critical points of $F(\mathbf{f})$ are found at the locations \mathbf{f}^c in which $\nabla F(\mathbf{f}^c) = 0$. We can write this condition in terms of R and S as

$$\nabla F(\mathbf{f}^c) = \frac{S(\mathbf{f}^c)\nabla R(\mathbf{f}^c) - R(\mathbf{f}^c)\nabla S(\mathbf{f}^c)}{S^2(\mathbf{f}^c)} = 0. \quad (\text{A } 3)$$

Rearranging the terms in (A 3) yields a form that assimilates the eigenproblem in (A 1) as

$$\nabla R(\mathbf{f}^c) - \frac{R(\mathbf{f}^c)}{S(\mathbf{f}^c)}\nabla S(\mathbf{f}^c) = 0, \quad (\text{A } 4)$$

where we have adopted $r(\mathbf{f}^c) = \nabla R(\mathbf{f}^c)$, $s(\mathbf{f}^c) = \nabla S(\mathbf{f}^c)$ and $\lambda = R(\mathbf{f}^c)/S(\mathbf{f}^c)$. Note that in order for this definition to hold, S must be continuously differentiable. In addition, in the case where $R(\mathbf{f})$ and $S(\mathbf{f})$ represent second-order functionals, (A 4) becomes a linear eigenproblem.

The nonlinear eigenproblem in (A 4) is solved using an inverse iteration, also referred to as inverse power method. For a linear operator A , this scheme takes the form $A\mathbf{f}^{k+1} = \mathbf{f}^k$, which is equivalent to the solution to the optimisation problem

$$\mathbf{f}^{k+1} = \arg \min_{\|\mathbf{f}\|_2 \leq 1} \left(\frac{1}{2} \langle \mathbf{f}, A\mathbf{u} \rangle - \langle \mathbf{f}, \mathbf{f}^k \rangle \right). \quad (\text{A } 5)$$

Considering the general eigenproblem presented in (A 1), the iterative scheme utilised in this work is written as

$$\mathbf{f}^{k+1} = \arg \min_{\|\mathbf{f}\|_2 \leq 1} \left(R(\mathbf{f}) - \langle \mathbf{f}, s(\mathbf{f}^k) \rangle \right). \quad (\text{A } 6)$$

According to the form of the eigenproblem shown in (A 4) the corresponding eigenvalue is computed as $\lambda^{k+1} = R(\mathbf{f}^{k+1})/S(\mathbf{f}^{k+1})$. Note that in our problem, the function $F(\mathbf{f})$ takes the form

$$F(\mathbf{f}) = \frac{(1 - \alpha)\|\mathbf{f}\|_2 + \alpha\|\mathbf{f}\|_1}{\|\mathcal{H}^* \mathbf{f}\|_2}, \quad (\text{A } 7)$$

for which the optimisation problem in (A 6) is rewritten as the following convex optimization problem

$$\mathbf{g}^{k+1} = \arg \min_{\|\mathbf{f}\|_2 \leq 1} [(1 - \alpha)\|\mathbf{f}\|_2 + \alpha\|\mathbf{f}\|_1 - \lambda^k \langle \mathbf{f}, \boldsymbol{\mu}^k \rangle], \quad (\text{A } 8)$$

where

$$\boldsymbol{\mu}^k = \frac{\Sigma \mathbf{f}^k}{\sqrt{\langle \mathbf{f}^k, \Sigma \mathbf{f}^k \rangle}}, \quad (\text{A } 9)$$

where for our problem, $\Sigma = \mathcal{H}\mathcal{H}^*$. This optimisation problem has the closed solution

$$\mathbf{g}_i^{k+1} = \frac{\text{sign}(\boldsymbol{\mu}_i^k)(\lambda^k |\boldsymbol{\mu}_i^k| - \alpha)_+}{s}, \quad (\text{A } 10)$$

with $s = \sqrt{\sum_{i=1}^n (\lambda^k |\boldsymbol{\mu}_i^k| - \alpha)_+^2}$ and $a_+ = \max(0, a)$. Notice that s now represents a scaling factor and is excluded from the method for simplicity. The algorithm that computes the optimal solution to the nonlinear eigenproblem in (A 4) using an inverse power method with the closed solution indicated in (A 10) for sparse resolvent analysis is presented in algorithm 2.

Algorithm 2 Inverse power method for sparse resolvent analysis

Input: Resolvent operator \mathcal{H} , sparsity controlling parameter α , accuracy ϵ

- 1: **Initialization:** \mathbf{f}^0 =random, with $\|\mathbf{f}^0\|_2 = 1$ and $\lambda^0 = F(\mathbf{f}^0)$
- 2: **while** $|\lambda^{k+1} - \lambda^k|/\lambda^k > \epsilon$ **do**
- 3: $\mathbf{g}_i^{k+1} = \text{sign}(\boldsymbol{\mu}_i^k)(\lambda^k |\boldsymbol{\mu}_i^k| - \alpha)_+$
- 4: $\mathbf{f}^{k+1} = \mathbf{g}^{k+1} / \|\mathcal{H}^* \mathbf{g}^{k+1}\|_2$
- 5: $\lambda^{k+1} = (1 - \alpha)\|\mathbf{f}^{k+1}\|_2 + \alpha\|\mathbf{f}^{k+1}\|_1$
- 6: $\boldsymbol{\mu}^{k+1} = \Sigma \mathbf{f}^{k+1} / \|\mathcal{H}^* \mathbf{f}^{k+1}\|_2$
- 7: **end while**

Output: raw sparse resolvent response modes $\boldsymbol{\psi}^{raw} = \mathbf{f}^{k+1}$

Appendix B. Convergence study of space-time resolvent analysis

This appendix contains convergence studies related to the results presented in this paper. In particular, a sweep was performed in a subset of the parameters N_y and N_t . The convergence of the methods was assessed in terms of the energy contained by the leading mode σ_1^2 , as well as the sum of the energy $\sum_i^n \sigma_i^2$ of the first $n = 10$ modes. Figures 16-17 shows the convergence of the results for the statistically-stationary channel flow configuration, while figures 18-19 provides analogous results for the Stokes boundary layer. For the channel flow with a lateral pressure gradient, convergence was studied through comparison with results of Ballouz *et al.* (2024), as discussed in §3.5. Our available computational power (1,500 GB RAM) provided a threshold in terms of the total grid size $N = N_y N_t$ for each configuration.

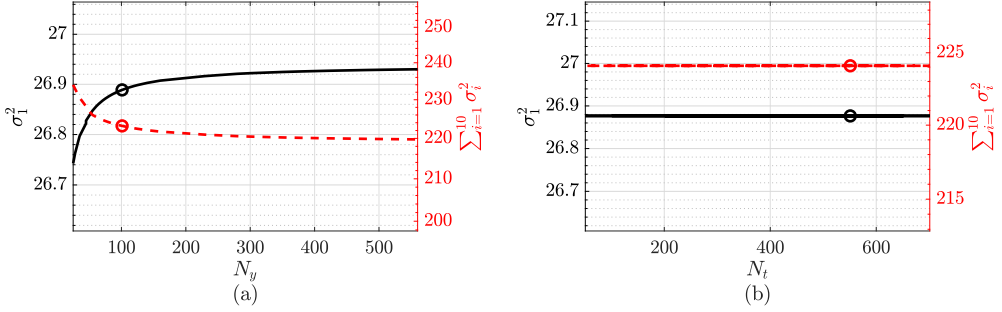


Figure 16: Evolution of σ_1^2 (black) and $\sum_{i=1}^{10} \sigma_i^2$ (red) as a function of (a) N_y for a constant total grid size $N = N_y N_t = 5.7 \times 10^4$, and (b) as a function of N_t for a constant spatial grid size $N_y = 81$ in the non-sparse implementation of space-time resolvent analysis for a turbulent channel flow $Re_\tau = 186$, and $\lambda_x^+ = 1000$, $\lambda_z^+ = 100$ for a time horizon $\tau_{tot} = 20\tau = 20(2\pi/\omega)$. Circles indicate resolution used in the rest of the paper.

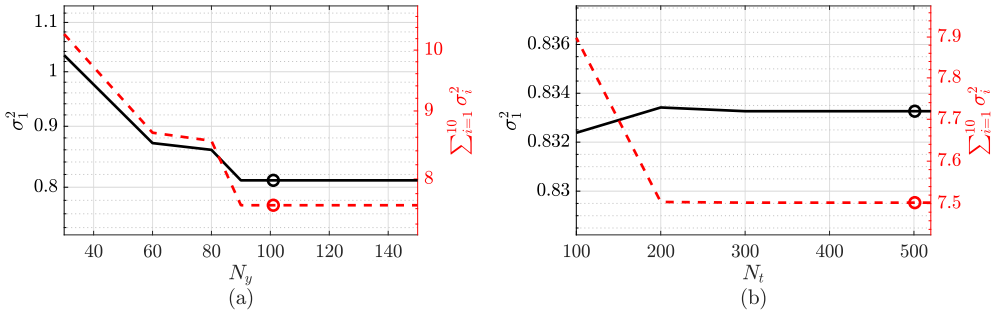


Figure 17: Evolution of σ_1^2 (black) and $\sum_{i=1}^{10} \sigma_i^2$ (red) as a function of N_y for a constant total grid size $N = N_y N_t = 5.4 \times 10^4$ (a) and (b) as a function of N_t for a constant spatial grid size $N_y = 101$, in the sparse implementation of space-time resolvent analysis for a turbulent channel flow $Re_\tau = 186$, and $\lambda_x^+ = 1000$, $\lambda_z^+ = 100$ with $\alpha = 0.001$ for a time horizon $\tau_{tot} = 20\tau = 20(2\pi/\omega)$. Circles indicate resolution used in the rest of the paper.

Note that the computational cost of the sparse formulation of the analysis is slightly higher, and therefore the maximum N is slightly lower in these cases. In all cases, as indicated by circles on the plots, we choose the resolution N_y and N_t such that adding additional resolution in either dimension has minimal effect on both the leading and the sum of the squares of the first ten singular values.

REFERENCES

- ABREU, L. I., CAVALIERI, A. V. G., SCHLATTER, P., VINUESA, R. & HENNINGSON, D. S. 2020 Spectral proper orthogonal decomposition and resolvent analysis of near-wall coherent structures in turbulent pipe flows. *J. Fluid. Mech.* **900**, A11.
- AKHAVAN, R., KAMM, R.D. & SHAPIRO, A.H. 1991 An investigation of transition to turbulence in bounded oscillatory Stokes flows part 1. experiments. *J. Fluid. Mech.* **225**, 395–422.
- BAE, H. J., DAWSON, S. T. M. & MCKEON, B. J. 2020a Resolvent-based study of compressibility effects on supersonic turbulent boundary layers. *J. Fluid. Mech.* **883**, A29.
- BAE, H. J., DAWSON, S. T. M. & MCKEON, B. J. 2020b Studying the effect of wall cooling in supersonic boundary layer flow using resolvent analysis. In *AIAA Scitech 2020 Forum*, p. 0575.

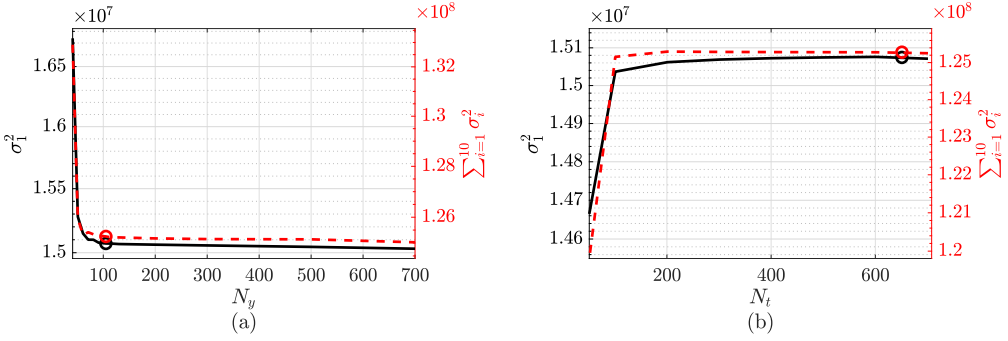


Figure 18: Evolution of σ_1^2 (black) and $\sum_{i=1}^{10} \sigma_i^2$ (red) as a function of (a) N_y for a constant total grid size $N = N_y N_t = 7.3 \times 10^4$, and (b) as a function of N_t for a constant spatial grid size $N_y = 81$, in the non-sparse implementation of space-time resolvent analysis for a turbulent Stokes boundary layer with $\lambda_x/h=0.471$ and $\lambda_z/h=0.236$ during a full oscillating cycle. Circles indicate resolution used in the rest of the paper.

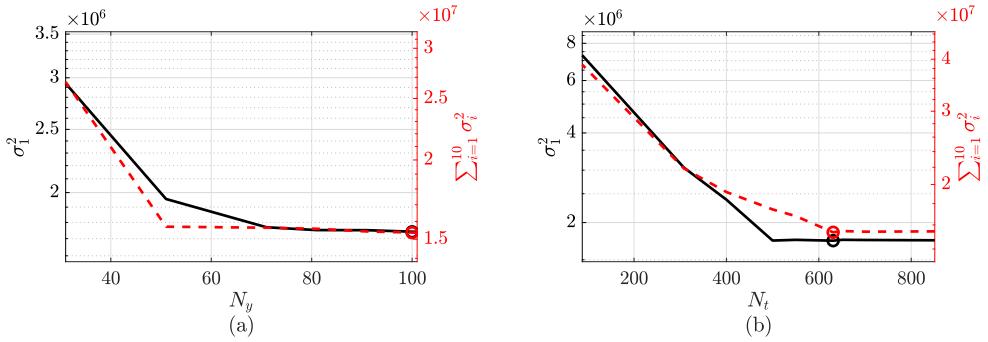


Figure 19: Evolution of σ_1^2 (black) and $\sum_{i=1}^{10} \sigma_i^2$ (red) as a function of (a) N_y for a constant total grid size $N = N_y N_t = 6.33 \times 10^4$, and (b) as a function of N_t for a constant spatial grid size $N_y = 81$, in the sparse implementation of space-time resolvent analysis for a turbulent Stokes boundary layer with $\lambda_x/h=0.471$ and $\lambda_z/h=0.236$ for $\alpha = 0.001$ during a full oscillating cycle. Circles indicate resolution used in the rest of the paper.

- BAE, H. J., LOZANO-DURAN, A., BOSE, S. T. & MOIN, P. 2018 Turbulence intensities in large-eddy simulation of wall-bounded flows. *Phys. Rev. Fluids* **3** (1), 014610.
- BAE, H. J., LOZANO-DURÁN, A., BOSE, S. T. & MOIN, P. 2019 Dynamic slip wall model for large-eddy simulation. *J. Fluid. Mech.* **859**, 400–432.
- BALLOUZ, E., LOPEZ-DORIGA, B., DAWSON, S. T. M. & BAE, H. J. 2023 Wavelet-based resolvent analysis of temporally-varying turbulent flows. *AIAA Scitech 2023 Forum* p. 0676.
- BALLOUZ, E., LOPEZ-DORIGA, B., DAWSON, S. T. M. & BAE, H. J. 2024 Wavelet-based resolvent analysis of non-stationary flows. *Submitted to J. Fluid. Mech.*
- BARKLEY, D., BLACKBURN, H. M. & SHERWIN, S. J. 2008 Direct optimal growth analysis for timesteppers. *Int. J. Numer. Methods Fluids* **57** (9), 1435–1458.
- BENEDDINE, S., YEGAVIAN, R., SIPP, D. & LECLAIRE, B. 2017 Unsteady flow dynamics reconstruction from mean flow and point sensors: an experimental study. *J. Fluid. Mech.* **824**, 174–201.
- BÖBERG, L. & BRÖSA, U. 1988 Onset of turbulence in a pipe. *Zeitschrift für Naturforschung A* **43** (8-9), 697–726.
- BRUNTON, S. L., PROCTOR, J. L. & KUTZ, J. N. 2016 Discovering governing equations from data by sparse identification of nonlinear dynamical systems. *PNAS* **113** (15), 3932–3937.
- BÜHLER, T. 2014 A flexible framework for solving constrained ratio problems in machine learning. PhD thesis, Saarland University.

- BUTLER, K. M. & FARRELL, B. F. 1992 Three-dimensional optimal perturbations in viscous shear flow. *Phys. Fluids A: Fluid Dynamics* **4** (8), 1637–1650.
- CANDÈS, E. J. & WAKIN, M. B. 2008 An introduction to compressive sampling. *IEEE Signal Process. Mag.* **25** (2), 21–30.
- CHAVARIN, A. & LUHAR, M. 2019 Resolvent analysis for turbulent channel flow with riblets. *AIAA Journal* pp. 1–11.
- COSTAMAGNA, P., VITTORI, G. & BLONDEAUX, P. 2003 Coherent structures in oscillatory boundary layers. *J. Fluid. Mech.* **474**, 1–33.
- DAWSON, S. T. M. & MCKEON, B. J. 2019 On the shape of resolvent modes in wall-bounded turbulence. *J. Fluid. Mech.* **877**, 682–716.
- DAWSON, S. T. M. & MCKEON, B. J. 2020 Prediction of resolvent mode shapes in supersonic turbulent boundary layers. *Int. J. Heat Fluid Fl.* **85**, 108677.
- DEL ALAMO, J. C. & JIMENEZ, J. 2006 Linear energy amplification in turbulent channels. *J. Fluid. Mech.* **559**, 205–213.
- DENNIS, D. J. C. & NICKELS, T. B. 2011 Experimental measurement of large-scale three-dimensional structures in a turbulent boundary layer. Part 1. Vortex packets. *J. Fluid. Mech.* **673**, 180–217.
- EDSTRAND, A. M., SCHMID, P. J., TAIRA, K. & CATTAFESTA, L. N. 2018 A parallel stability analysis of a trailing vortex wake. *J. Fluid. Mech.* **837**, 858–895.
- FARGHADAN, A., MARTINI, E. & TOWNE, A. 2023 Scalable resolvent analysis for three-dimensional flows. *arXiv preprint arXiv:2309.04617* .
- FOURES, D. P. G., CAULFIELD, C. P. & SCHMID, P. J. 2013 Localization of flow structures using-norm optimization. *J. Fluid. Mech.* **729**, 672–701.
- FRAME, P. & TOWNE, A. 2022 Space-time POD and the Hankel matrix. *arXiv preprint arXiv:2206.08995* .
- GÓMEZ, F., BLACKBURN, H. M., RUDMAN, M., SHARMA, A. S. & MCKEON, B. J. 2016 A reduced-order model of three-dimensional unsteady flow in a cavity based on the resolvent operator. *J. Fluid. Mech.* **798**, R2.
- HEAD, M. R. & BANDYOPADHYAY, P. 1981 New aspects of turbulent boundary-layer structure. *J. Fluid. Mech.* **107**, 297–338.
- HEIDT, L. & COLONIUS, T. 2023 Spectral proper orthogonal decomposition of harmonically forced turbulent flows. *arXiv preprint arXiv:2305.05628* .
- HEIN, M. & BÜHLER, T. 2010 An inverse power method for nonlinear eigenproblems with applications in 1-spectral clustering and sparse PCA. *Adv Neural Inf Process Syst* **23** (NIPS 2010).
- HINO, M., SAWAMOTO, M. & TAKASU, S. 1976 Experiments on transition to turbulence in an oscillatory pipe flow. *J. Fluid. Mech.* **75** (2), 193–207.
- HUTCHINS, N. & MARUSIC, I. 2007 Evidence of very long meandering features in the logarithmic region of turbulent boundary layers. *J. Fluid. Mech.* **579**, 1–28.
- HWANG, Y. & COSSU, C. 2010 Linear non-normal energy amplification of harmonic and stochastic forcing in the turbulent channel flow. *J. Fluid. Mech.* **664**, 51–73.
- ILLINGWORTH, S. J., MONTY, J. P. & MARUSIC, I. 2018 Estimating large-scale structures in wall turbulence using linear models. *J. Fluid. Mech.* **842**, 146–162.
- JIMÉNEZ, J. 2018 Coherent structures in wall-bounded turbulence. *J. Fluid. Mech.* **842**, P1.
- JIMÉNEZ, J. & PINELLI, A. 1999 The autonomous cycle of near-wall turbulence. *J. Fluid. Mech.* **389**, 335–359.
- JOLLIFFE, I. T., TRENDAFILOV, N. T. & UDDIN, M. 2003 A modified principal component technique based on the LASSO. *JCGS* **12** (3), 531–547.
- JOURNÉE, M., NESTEROV, Y., RICHTÁRIK, P. & SEPULCHRE, R. 2010 Generalized power method for sparse principal component analysis. *J. Mach. Learn. Res.* **11** (2), 517–553.
- JOVANOVIĆ, M. R. & BAMIEH, B. 2005 Componentwise energy amplification in channel flows. *J. Fluid. Mech.* **534**, 145–183.
- JOVANOVIĆ, M. R., SCHMID, P. J. & NICHOLS, J. W. 2014 Sparsity-promoting dynamic mode decomposition. *Phys. Fluids* **26** (2).
- KERN, J. S., BENEITEZ, M., HANIFI, A. & HENNINGSON, D. S. 2021 Transient linear stability of pulsating poiseuille flow using optimally time-dependent modes. *J. Fluid Mech.* **927**, A6.
- KIM, J. & MOIN, P. 1985 Application of a fractional-step method to incompressible Navier-Stokes equations. *J. Comput. Phys.* **59** (2), 308–323.
- KIM, K. C. & ADRIAN, R. J. 1999 Very large-scale motion in the outer layer. *Phys. Fluids* **11** (2), 417–422.

- KLINE, S. J., REYNOLDS, W. C., SCHRAUB, F. A. & RUNSTADLER, P. W. 1967 The structure of turbulent boundary layers. *J. Fluid. Mech.* **30** (4), 741–773.
- LANDAHL, M. T. 1975 Wave breakdown and turbulence. *SIAM Journal on Applied Mathematics* **28** (4), 735–756.
- LANDAHL, M. T. 1980 A note on an algebraic instability of inviscid parallel shear flows. *J. Fluid. Mech.* **98** (2), 243–251.
- LESSHAFFT, L., SEMERARO, O., JAUNET, V., CAVALIERI, A. V. G. & JORDAN, P. 2019 Resolvent-based modeling of coherent wave packets in a turbulent jet. *Phys. Rev. Fluids* **4** (6), 063901.
- LIN, C.-T., TSAI, M.-L. & TSAI, H.-C. 2023 Flow control of a plunging cylinder based on resolvent analysis. *J. Fluid. Mech.* **967**, A41.
- LOISEAU, J.-C. & BRUNTON, S. L. 2018 Constrained sparse Galerkin regression. *J. Fluid. Mech.* **838**, 42–67.
- LOPEZ-DORIGA, B., BALLOUZ, E., BAE, H. J. & DAWSON, S. T. M. 2023 A sparsity-promoting resolvent analysis for the identification of spatiotemporally-localized amplification mechanisms. *AIAA Scitech 2023 Forum* p. 0677.
- LOPEZ-DORIGA, B., DAWSON, S. T. M. & VINUESA, R. 2022 Resolvent analysis of laminar and turbulent rectangular duct flows. *AIAA Aviation 2022 Forum* p. 3334.
- LOZANO-DURÁN, A. & BAE, H. J. 2019 Characteristic scales of townsend’s wall-attached eddies. *J. Fluid. Mech.* **868**, 698–725.
- LOZANO-DURÁN, A., GIOMETTO, M. G., PARK, G. I., & MOIN, P. 2020 Non-equilibrium three-dimensional boundary layers at moderate reynolds numbers. *J. Fluid. Mech.* **883**, A20.
- LUHAR, M., SHARMA, A. S. & McKEON, B. J. 2014 Opposition control within the resolvent analysis framework. *J. Fluid. Mech.* **749**, 597–626.
- LUHAR, M., SHARMA, A. S. & McKEON, B. J. 2015 A framework for studying the effect of compliant surfaces on wall turbulence. *J. Fluid. Mech.* **768**, 415–441.
- MAO, X. & SHERWIN, S. J. 2011 Continuous spectra of the Batchelor vortex. *J. Fluid. Mech.* **681**, 1–23.
- MARTINI, E., CAVALIERI, A. V. G., JORDAN, P., TOWNE, A. & LESSHAFFT, L. 2020 Resolvent-based optimal estimation of transitional and turbulent flows. *J. Fluid. Mech.* **900**, A2.
- McKEON, B. J. 2017 The engine behind (wall) turbulence: perspectives on scale interactions. *J. Fluid. Mech.* **817**, P1.
- McKEON, B. J. & SHARMA, A. S. 2010 A critical-layer framework for turbulent pipe flow. *J. Fluid. Mech.* **658**, 336–382.
- McMULLEN, R. M., ROSENBERG, K. & McKEON, B. J. 2020 Interaction of forced Orr-Sommerfeld and Squire modes in a low-order representation of turbulent channel flow. *Phys. Rev. Fluids* **5** (8), 084607.
- MESEGUER, Á. & TREFETHEN, L.N. 2003 Linearized pipe flow to Reynolds number 10^7 . *J. Comput. Phys.* **186**, 178–197.
- MOARREF, R., SHARMA, A. S., TROPP, J. A. & McKEON, B. J. 2013 Model-based scaling of the streamwise energy density in high-Reynolds-number turbulent channels. *J. Fluid. Mech.* **734**, 275–316.
- MOIN, P., SHIH, T.-H., DRIVER, D. M. & MANSOUR, N. N. 1990 “Direct numerical simulation of a three-dimensional turbulent boundary layer. *Phys. Fluids* **2**, 1846–1853.
- OBRIST, D. & SCHMID, P. J. 2010 Algebraically decaying modes and wave packet pseudo-modes in swept Hiemenz flow. *J. Fluid. Mech.* **643**, 309–332.
- OBRIST, D. & SCHMID, P. J. 2011 Algebraically diverging modes upstream of a swept bluff body. *J. Fluid. Mech.* **683**, 346–356.
- ORLANDI, P. 2000 *Fluid flow phenomena: a numerical toolkit*. Springer Science & Business Media.
- ORR, W. M’F. 1907 The stability or instability of the steady motions of a perfect liquid and of a viscous liquid. Part II: A viscous liquid. In *Proc. R. Ir. Acad. A*, pp. 69–138. JSTOR.
- PADOVAN, A., OTTO, S. & ROWLEY, C. 2020 Analysis of amplification mechanisms and cross-frequency interactions in nonlinear flows via the harmonic resolvent. *J. Fluid. Mech.* **900**, A14.
- PADOVAN, A. & ROWLEY, C. W. 2022 Analysis of the dynamics of subharmonic flow structures via the harmonic resolvent: Application to vortex pairing in an axisymmetric jet. *Phys. Rev. Fluids* **7** (7), 073903.
- PICKERING, E., TOWNE, A., JORDAN, P. & COLONIUS, T. 2021 Resolvent-based modeling of turbulent jet noise. *J. Acoust. Soc. Am.* **150** (4), 2421–2433.
- PIER, B. & SCHMID, P. J. 2017 Linear and nonlinear dynamics of pulsatile channel flow. *J. Fluid Mech.* **815**, 435–480.

- REDDY, S. C. & HENNINGSON, D. S. 1993 Energy growth in viscous channel flows. *J. Fluid. Mech.* **252**, 209–238.
- ROSENBERG, K. & McKEON, B. J. 2019 Efficient representation of exact coherent states of the Navier–Stokes equations using resolvent analysis. *Fluid Dyn. Res.* **51**, 011401.
- RUBINI, R., LASAGNA, D. & DA RONCH, A. 2020 The l_1 -based sparsification of energy interactions in unsteady lid-driven cavity flow. *J. Fluid. Mech.* **905**, A15.
- SCHMID, P. J. 2007 Nonmodal stability theory. *Annu. Rev. Fluid Mech.* **39**, 129–62.
- SCHMID, P. J. & HENNINGSON, D. S. 2001 *Stability and Transition in Shear Flows*. Springer, New York, NY.
- SCHMIDT, O. T. & SCHMID, P. J. 2019 A conditional space–time POD formalism for intermittent and rare events: example of acoustic bursts in turbulent jets. *J. Fluid. Mech.* **867**, R2.
- SCHOPPA, W. & HUSSAIN, F. 2002 Coherent structure generation in near-wall turbulence. *J. Fluid. Mech.* **453**, 57–108.
- SHARMA, A. S. & McKEON, B. J. 2013 On coherent structure in wall turbulence. *J. Fluid. Mech.* **728**, 196–238.
- SHARMA, A. S., MOARREF, R. & McKEON, B. J. 2017 Scaling and interaction of self-similar modes in models of high-Reynolds number wall turbulence. *Phil. Trans. R. Soc. A* **375** (2089), 20160089.
- SIGG, C. D. & BUHMANN, J. M. 2008 Expectation-maximization for sparse and non-negative pca. In *ICML 2008*, pp. 960–967.
- SILLERO, J. A., JIMENEZ, J. & MOSER, R. D. 2014 Two-point statistics for turbulent boundary layers and channels at reynolds numbers up to $\delta^+ \approx 2000$. *Phys. Fluids* **26**.
- SKENE, C. S., YEH, C.-A., SCHMID, P. J. & TAIRA, K. 2022 Sparsifying the resolvent forcing mode via gradient-based optimisation. *J. Fluid. Mech.* **944**, A52.
- SYMON, S., SIPP, D., SCHMID, P. J. & McKEON, B. J. 2019 Mean and unsteady flow reconstruction using data-assimilation and resolvent analysis. *AIAA Journal* pp. 1–14.
- THEODORSEN, T. 1952 Mechanisms of turbulence. In *In Proc. 2nd Midwestern Conf. of Fluid Mechanics, Ohio State University.*
- TISSOT, G., CAVALIERI, A. V. G. & MÉMIN, E. 2021 Stochastic linear modes in a turbulent channel flow. *J. Fluid. Mech.* **912**, A51.
- TOEDTLI, S. S., LUHAR, M. & McKEON, B. J. 2019 Predicting the response of turbulent channel flow to varying-phase opposition control: Resolvent analysis as a tool for flow control design. *Phys. Rev. Fluids* **4** (7), 073905.
- TOWNE, A., LOZANO-DURÁN, A. & YANG, X. I. A. 2020 Resolvent-based estimation of space-time flow statistics. *J. Fluid. Mech.* **883**, A17.
- TOWNE, A., SCHMIDT, O. T. & COLONIUS, T. 2018 Spectral proper orthogonal decomposition and its relationship to dynamic mode decomposition and resolvent analysis. *J. Fluid. Mech.* **847**, 821–867.
- TU, J. H., ROWLEY, C. W., KUTZ, J. N. & SHANG, J. K. 2014 Spectral analysis of fluid flows using sub-Nyquist-rate PIV data. *Exp. Fluids* **55** (9), 1–13.
- VERZICCO, R & VITTORI, G 1996 Direct simulation of transition in stokes boundary layers. *Phys. Fluids* **8** (6), 1341–1343.
- VITTORI, G & VERZICCO, R 1998 Direct simulation of transition in an oscillatory boundary layer. *J. Fluid. Mech.* **371**, 207–232.
- WEIDEMAN, J. A. & REDDY, S. C. 2000 A Matlab differentiation matrix suite. *TOMS* **26** (4), 465–519.
- WRAY, A. A. 1990 Minimal storage time advancement schemes for spectral methods. *NASA Ames Research Center, California, Report No. MS 202*.
- YEH, C.-A. & TAIRA, K. 2019 Resolvent-analysis-based design of airfoil separation control. *J. Fluid. Mech.* **867**, 572–610.
- ZARE, A., JOVANOVIĆ, M. R. & GEORGIU, T. T. 2017 Colour of turbulence. *J. Fluid. Mech.* **812**, 636–680.
- ZOU, H., HASTIE, T. & TIBSHIRANI, R. 2006 Sparse principal component analysis. *JCGS* **15** (2), 265–286.
- ZOU, H. & XUE, L. 2018 A selective overview of sparse principal component analysis. *Proc. IEEE* **106** (8), 1311–1320.